Inhibition of the renal apical sodium dependent bile acid transporter prevents cholemic nephropathy in mice with obstructive cholestasis

Ahmed Ghallab, Daniela González, Ellen Strängberg, Ute Hofmann, Maiju Myllys, Reham Hassan, Zaynab Hobloss, Lisa Brackhagen, Brigitte Begher-Tibbe, Julia Duda, Carolin Drenda, Franziska Kappenberg, Joerg Reinders, Adrian Friebel, Mihael Vucur, Monika Turajski, Abdel-latief Seddek, Tahany Abbas, Noha Abdelmageed, Samy A.F. Morad, Walaa Morad, Amira Hamdy, Wiebke Albrecht, Naim Kittana, Mohyeddin Assali, Nachiket Vartak, Christoph van Thriel, Ansam Sous, Patrick Nell, Maria Villar-Fernandez, Cristina Cadenas, Erhan Genc, Rosemarie Marchan, Tom Luedde, Peter Åkerblad, Jan Mattsson, Hanns-Ulrich Marschall, Stefan Hoehme, Guido Stirnimann, Matthias Schwab, Peter Boor, Kerstin Amann, Jessica Schmitz, Jan H. Bräsen, Jörg Rahnenführer, Karolina Edlund, Saul J. Karpen, Benedikt Simbrunner, Thomas Reiberger, Mattias Mandorfer, Michael Trauner, Paul A. Dawson, Erik Lindström, Jan G. Hengstler

Table of contents

Supplementary methods

Renal biopsies of patients with cholemic nephropathy. A total number of 21 and 11 renal biopsies from CN and non-CN patients, respectively, were collected from two cohorts, the Hannover cohort (14 CN and 4 non-CN biopsies) and the Erlangen cohort (7 CN and 7 non-CN biopsies) (Table S1). The study was conducted according to the ethical guidelines of the 1975 Helsinki Declaration and was approved by the local ethics committee (no. 4415, 22-150-D).

Animals and bile duct ligation. Eight-to-10-week-old male and female C57BL/6N (Janvier Labs, France) or *Cyp2c70*$^{-/-}$ and corresponding C57BL/6J wildtype (Dawson, Karpen Lab) mice were used. The mice were housed at standard environmental conditions with free access to water, and ad libitum feeding with Ssniff R/M-H, 10 mm standard diet (Ssniff, Soest, Germany). All experiments were approved by the local animal welfare committee (LANUV, North Rhine-Westphalia, Germany, application number: 81-02.04.2022.A286). To induce obstructive cholestasis the extrahepatic common bile duct was ligated at a position between the gallbladder and the duodenum, as previously described [1, 2].

Preparation and application of AS0369. A stock formulation was prepared by dissolving AS0369 in the vehicle solution (0.5% methyl cellulose and 0.06% Tween 80) followed by sonication and vortexing for several minutes until a uniform suspension was obtained. The different doses of 15, 30, 60 and 120 mg/kg b.w. were prepared by diluting the stock formulation accordingly in the vehicle solution. The ASBT inhibitor (AS0369) and the vehicle were administered orally by gavage twice per day with an application volume of 4 mL/kg b.w.

Sample collection and processing. Blood sampling. Heart blood samples were collected from anaesthetised mice in syringes precoated with disodium ethylenediaminetetraacetic acid (EDTA), as previously described [3]. After centrifugation, plasma was separated and stored at -80 °C until used for analysis. ***Tissue sample collection.*** Prior to tissue collection, transcardial perfusion with PBS was performed to wash out the remaining blood. *Liver tissue sample collection:* the whole liver was excised.

Samples of 5 × 7 mm diameter were collected from the left liver lobe and fixed for two days in 4% paraformaldehyde (PFA) followed by washing in PBS and embedding in paraffin. In addition, samples of 5 × 7 mm diameter were collected from the left liver lobe, immediately frozen in liquid nitrogen and stored at -80 °C until analysis by MALDI-MSI. The remaining liver tissue was snap-frozen by freeze-clamping and milling in liquid nitrogen, and subsequently stored at -80 °C until RNA isolation. *Kidney tissue sample collection:* both the left and the right kidneys were excised. After removal of the surrounding capsule, the right kidney was divided longitudinally into two halves; one half was fixed in 4% PFA and embedded in paraffin, and the other half was immediately frozen in liquid nitrogen and stored at -80 °C until analysis by MALDI-MSI. The left kidney was snap-frozen by freeze-clamping and milling in liquid nitrogen, and subsequently stored at -80 °C until RNA isolation. ***Urine sample collection.*** 24-hour urine samples were collected in metabolic cages as previously described [4]. Spontaneous urine samples were collected from female mice using a urinary bladder canula (25 gauge; SAI Infusion Technologies) as previously described [5]. ***Bile sample collection.*** Bile samples were collected from the gallbladder.

Biochemical analysis. Creatinine, urea, total bilirubin, and direct bilirubin from plasma and/or urine were determined using a C400 clinical chemistry analyzer (Pentra C400 Option I.S.E, HORIBA ABX SAS, Montpellier, France). Biomarkers of liver damage (alanine transaminase, aspartate transaminase and alkaline phosphatase) were measured in mouse plasma using the Piccolo Xpress Chemistry Analyzer (Hitado, Germany) and the Piccolo General Chemistry 13 Panel Kit. The plasma samples from control and BDL mice were diluted 1:1 or 1:5 in normal mouse serum (S7273 -50ML, Sigma-Aldrich), respectively, prior to analysis. AS0369 was analyzed in plasma and tissue samples using LC-MS/MS. ***Quantification of bile acids with LC-MS/MS.*** Bile acid concentrations in plasma, urine, bile, liver tissue and kidney tissue were determined by negative electrospray (ESI) liquid chromatography tandem mass spectrometry (LC-MS/MS) in multiple-reaction-monitoring (MRM) mode on an Agilent 6495B triple quadrupole mass spectrometer (Agilent, Germany) coupled to an Agilent Infinity II HPLC system as described previously [1]. Briefly, frozen tissue samples were homogenized in methanol: water 1:1 (v/v) in a FastPrep® 24 homogenizer (MP Biomedicals, Santa Ana,

USA) to a final concentration of 40 mg wet tissue/ml as described previously [6]. Aliquots of 5 µL of plasma or diluted bile (1:100), 30 µl of tissue homogenate, or 2 µl of urine were spiked with internal standard solution followed by protein precipitation with methanol and centrifugation. The supernatant was used for LC-MS/MS analysis. Urine samples above the calibration range were diluted with water 1:10 v/v to 1:50 v/v. LC-MS/MS parameters for measurement of bile acids and the internal standards are summarized in Table S2. Protein determination in tissue homogenates was performed with the PierceTM BCA protein assay kit.

ELISA assays: Determination of NGAL concentrations Concentrations of NGAL/Lcn-2 were determined in mouse urine and plasma using the Mouse Lipocalin-2/NGAL DuoSet ELISA kit plus the DuoSet ELISA Ancillary Reagent Kit 2 from R&D systems (DY1857 and DY008) according to the manufacturer's protocol. The concentrations of NGAL/Lcn-2 in human serum were determined using the Human Lipocalin-2/NGAL Quantikine ELISA kit from R&D Systems (DLCN20) following the manufacturer's protocol. The optical density of the color-forming TMB substrate from both assays was measured at 450 nm using a microplate reader (Infinite M200 Pro, Tecan) and the concentration of NGAL/Lcn-2 of each sample was calculated from the standard curve. ***Determination of Kim-1 concentrations.*** Concentrations of Kim-1 were determined in mouse urine and plasma using the Mouse KIM 1 ELISA Kit from Abcam (ab213477) according to the manufacturer's protocol. The concentrations of Kim-1 in human serum were determined using the Human Serum TIM-1/KIM-1 HAVCR Quantikine ELISA kit from R&D Systems (DSKM100). The optical density of the color-forming TMB substrate from both assays was measured at 450 nm using a microplate reader (Infinite M200 Pro, Tecan) and the concentration of KIM-1 of each sample was calculated from the standard curve. ***Determination of cystatin C concentrations.*** Concentrations of Cystatin C were determined in plasma using the Mouse Cystatin C ELISA Kit from Abcam (ab201280) according to manufacturer's protocol. For human serum samples the Human Cystatin C Quantikine ELISA kit from R&D Systems (DSCTC0) was used following the manufacturer's instructions. The optical density of the color forming TMB substrate from both assays was measured at 450 nm using a microplate reader (Infinite M200 Pro,

Tecan) and the concentration of Cystatin C of each sample was calculated from the standard curve.

Determination of IC_{50} of AS0369. Mouse IBAT- (10,000 cells) or LBAT- (20,000 cells) overexpressing cells were seeded in 96-well plates in 200 µl MEM-alpha medium supplemented with 10% FBS containing Puromycin (10 µg/ml) and incubated at 37°C in 5% CO_2 for 48 hrs. The incubation medium was decanted from the wells and cells were washed two times with 300 µl of basal MEM-alpha medium (FBS-free). Each time after decanting the medium, plates were tapped against paper towel to ensure maximum removal of residual media. Test inhibitor dilutions (highest test concentration being 10 µM, 3-fold serial dilution, 10 points) prepared in DMSO were added in incubation mix (maintaining 0.2% final DMSO concentration) containing 0.25 µM 3H-Taurocholic acid and 5 µM of cold taurocholic acid. 50 µl of incubation mix containing test inhibitors was then added to the wells (in duplicate) and the plates were incubated for 20 min in a CO_2 incubator at 37°C. After incubation, the reaction was stopped by keeping the plates on ice water mix for 2-3 minutes and then the incubation mix was aspirated completely from the wells. The wells were washed two times with 250 µl of chilled unlabeled 1 mM taurocholic acid dissolved in HEPES-buffered (10 mM) HBSS (pH 7.4). The plates were tapped against a paper towel after every washing step to ensure maximum removal of blocking buffer. 100 µl of MicroScint-20 was added to the wells and kept overnight at room temperature before reading the plates in TopCount NXT™ Microplate Scintillation and Luminescence Counter from PerkinElmer under 3H Test protocol (set at 120 seconds reading time per well).

Histopathology. Hematoxylin and eosin (H&E) and Sirius red staining were performed in 4 µm thick PFA (4%)-fixed paraffin-embedded liver and kidney tissue sections. Hematoxylin staining was performed using the Discovery Ultra Automated Slide Preparation System, as previously described [7]. Eosin staining was performed according to a standard protocol [3]. Sirius red staining was done using a commercially available kit, according to the manufacturer's instructions. To visualize bilirubin casts in kidney tissues, Hall's staining was performed using 4 µm-thick PFA (4%)-fixed paraffin-embedded kidney tissue sections using a commercially available kit (StatLab), according to the

manufacturer's instructions. The principle of this staining technique is that oxidation of bilirubin in acidic medium results in formation of biliverdin which can be distinguished by its green color [8]; the cell cytoplasm stains yellow, while collagen appears red.

Immunohistochemistry. Immunostainings were performed using 4 µm-thick PFA (4%)-fixed paraffin-embedded liver and/or kidney tissue sections using the Discovery Ultra Automated Slide Preparation System, as previously described [9, 10]. Antibodies and their concentrations are given in Table S3. Nuclei were visualized by counter-staining with Mayer's hematoxylin. Whole slide scanning was performed using the Axio Scan.Z1.

Image analysis. High-resolution whole slide scans (~1 Gpixel each) were preprocessed using CLAHE, a widely used image processing technique improving the contrast in images by stretching the intensity distribution of the pixels [11] implemented in the software TiQuant [12]. The resulting data was segmented in a two-step process, starting with a Random Forest classification [13] to distinguish tissue and non-tissue regions, and a region of interest within the tissue typically emphasized by staining. Random forest classification is an accurate and robust machine learning technique, whereby features are chosen based on the highest information gain. The model to classify each pixel was manually trained by a subset of images for each staining but was applied to all images using the software QuPath [14]. In a second segmentation step, we refined the segmentation result using the TiQuant software by a semantically informed application of morphological operators that considered known structure shape, size, and localization in tissue to further improve the segmentation accuracy. The diameter of the bile canaliculi network was measured using a pruned skeletonization of the bile network segmentation by averaging the diameter of the maximally inscribed spheres along the skeleton[15].

Intravital imaging. Functional intravital imaging of livers and kidneys of anesthetised mice was performed using an inverted two-photon microscope LSM MP7 or LSM880 (Zeiss, Germany), as previously described [9, 16-18]. Before recording, the mice received bolus tail vein injections of Hoechst 33258 (nuclear marker), TMRE (mitochondrial membrane potential marker), SYTOX green (cell death marker), 2',7'dichlorofluorescein diacetate (H_2DCFDA; a non-fluorescent probe that passes passively into cells, de-esterified intracellularly, and turns to the green-fluorescent dichlorofluorescein (DCF) upon oxidation) and/or anti-CD31 antibody (endothelial cell marker) (Table S4). To allow

administration of further functional dyes/markers while recording, a mouse catheter (SAI-infusion, IL, USA) was fixed in the tail vein. To analyse bile flux in the liver and kidneys, fluorescently labelled taurocholic acid (TCA) or the bile acid analogue CLF was administered via the tail vein catheter as a bolus (Table S4) [9]. To check the integrity of peritubular capillaries, a bolus of the leakiness marker Evans blue [19] was administered and intravital recording was done using the LSM880 confocal microscope (Table S4). At least three mice were analysed for each of the experimental scenarios shown in the result section.

Video analysis. As preprocessing for quantification of intravital imaging, rigid-body registration was performed using StackReg [20] to compensate for tissue motion (e.g., due to respiration and heartbeat) in the time series. Two-dimensional projections were created from these stabilized videos by z-projection using the average, maximum, and standard deviation operators. The autocontext segmentation workflow of the ilastik interactive image segmentation software (version 1.3.3post1) [20] was used to segment the tissue compartments in these 2D projections. The analyzed compartments were peritubular capillaries and TMRE positive tubular epithelial cells in the kidney time series showing TCA uptake, and capillaries and interstitium in the time series visualizing Evans blue dynamics. In the liver, the considered compartments were sinusoidal capillaries, hepatocytes, and bile canaliculi showing TCA flux. Mean raw TCA / Evans blue intensities were measured per compartment and frame. Additionally, the mean TCA signal in the TMRE positive cell compartment was measured per tubule, and tubules were subsequently separated into two groups based on their maximum mean TCA intensity over time using k-means clustering.

Synthesis of TCA-FITC

TCA-FITC was synthetized according to the following scheme:

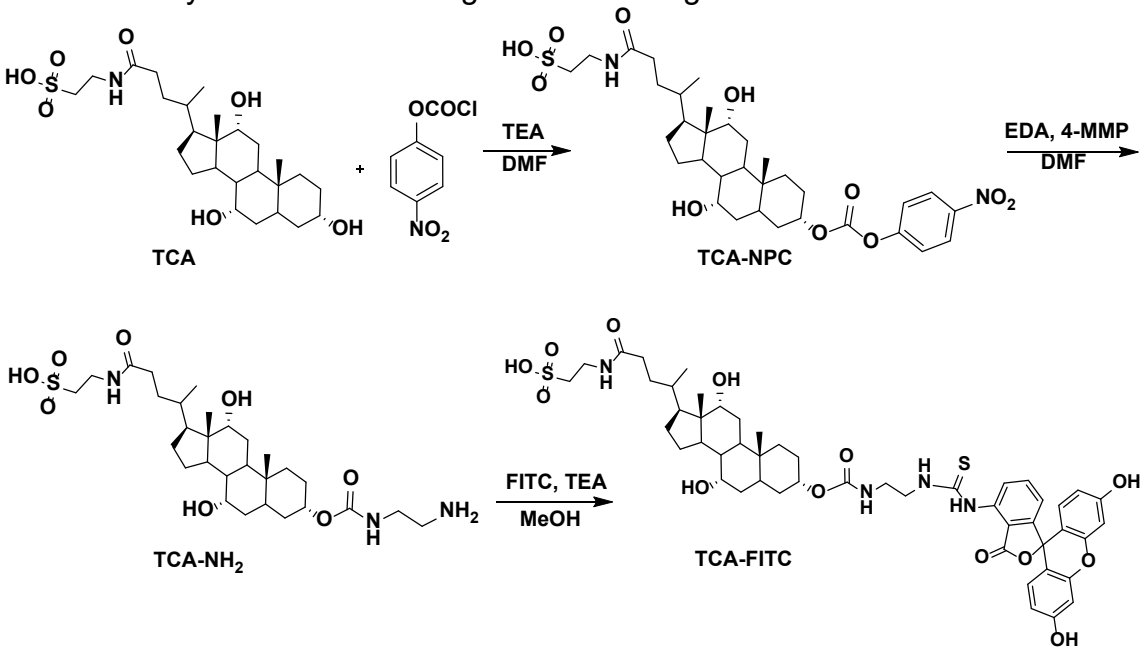

Synthesis of TCA-NPC. A mixture of taurocholic acid (250 mg, 0.465 mmol), 4-nitrophenyl chloroformate (4-NPC) (465 mg, 2.31 mmol), and triethylamine (TEA) (0.5 ml) in DMF (2.5 ml) was stirred at 0 °C for one hour under argon and then, the reaction was left at room temperature for the next day. The crude product was purified by the addition of ethyl acetate (30 ml) in an ice bath to obtain yellowish precipitation separated by centrifugation for 10 mins at 4000 rpm. The precipitate was washed three times with ethyl acetate and then dried under vacuum. The obtained product was dissolved in water and then lyophilized to obtain a white powder with a yield of 90%. ***Synthesis of TCA-NH2.*** To a solution of TCA-NPC (325 mg, 0.48 mmol) in DMF (4 ml), 4-methyl morpholine (4-MMP) (0.11 ml, 0.96 mmol) was added at 50 °C and left stirred for one hour. Then, ethylenediamine (EDA) (3.22 ml, 48.1 mmol) was added dropwise at room temperature for 30 mins and the reaction was left for the next day. The reaction was evaporated, and acetonitrile was added to remove the unreacted 4-MMP and EDA and the product was precipitated and filtrated. The precipitated product was redissolved in 1M DMF and recrystallized by the addition of ethyl acetate and dried under vacuum. The yield was 92%

with an R_f = 0.25 (DCM:MeOH 5:1) stained by ninhydrin. ***Synthesis of TCA-FITC.*** A solution of TCA-NH2 (50 mg, 0.05 mmol) in anhydrous methanol (1.5 ml) was added to a solution of FITC (29 mg, 0.075 mmol), TEA (0.2 ml) in anhydrous methanol (2.5 ml) under argon and stirred at 45 °C for 24 hours. After that, the reaction was evaporated and purified by column chromatography with a mobile phase DCM: MeOH (5:1) with a yield of 60%. The ^{1}H NMR spectrum confirms the successful synthesis of the TCA-FITC as in the figure below:

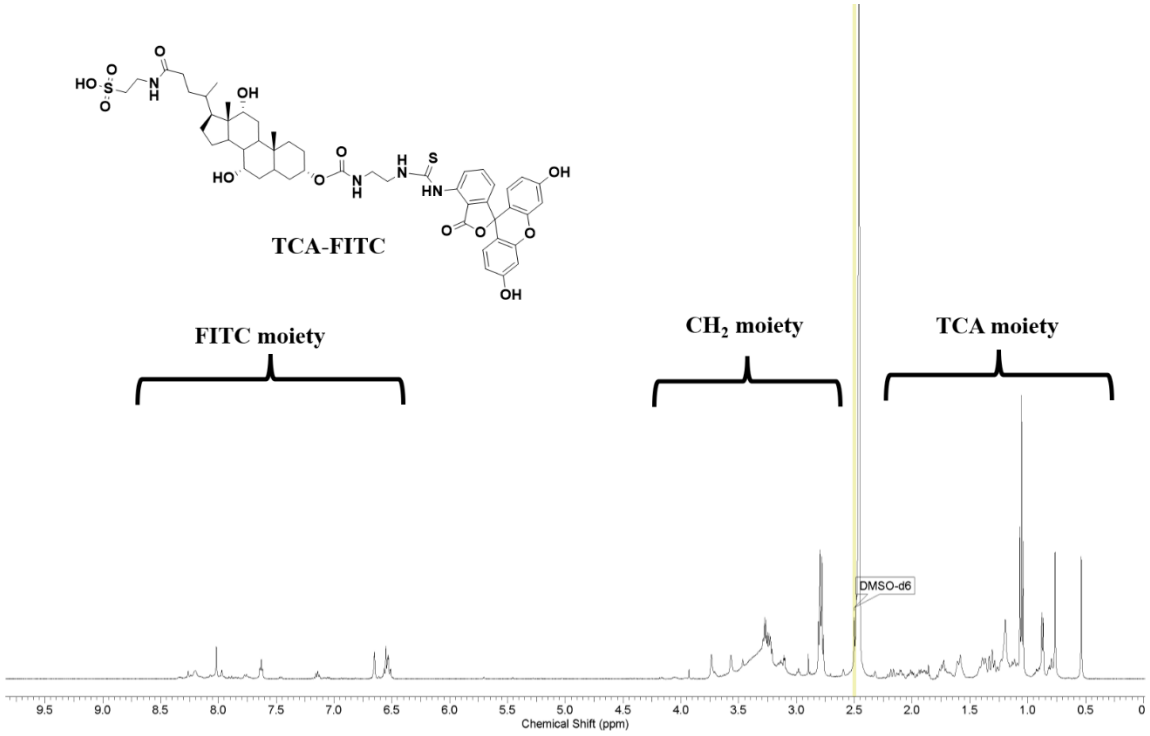

The chemical structure of the FITC-labelled taurocholic acid is given in the figure below:

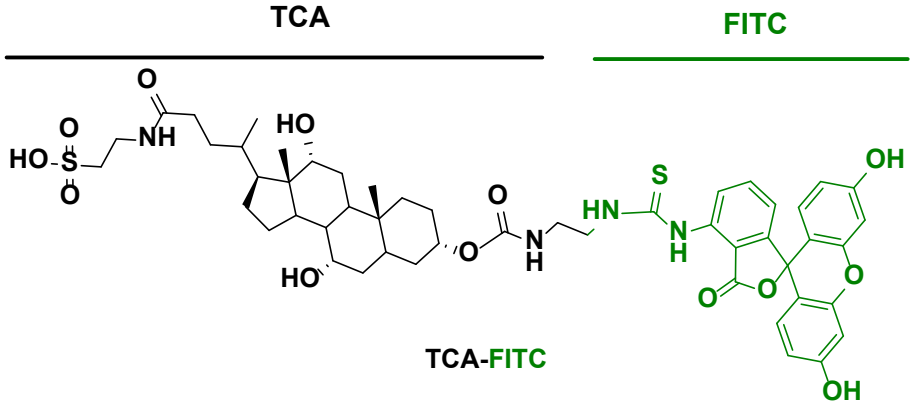

MALDI-MS-Imaging. Frozen specimens were sectioned serially into 5-µm-thick tissue sections using a Leica CM 3050 S cryostat. The sections were thaw-mounted on IntelliSlides (Bruker Daltonics, Bremen, Germany), dried in a desiccator, and stored at -20 °C until analysis. The tissue sections were sprayed (4 layers) with 5 mg/mL 2-mercaptobenzothiazole in acetone/water (5:1) using an HTX Imaging-Sprayer (HTX Technologies LLC, Chapel Hill, NC, USA) at 65 °C at 10 psi nitrogen. The flow was 120 µL/min. MALDI-measurements were accomplished on MS1-level in negative mode with a tims TOF FleX without ion-mobility separation in a mass range from 85-800 m/z and calibrated internally using the 2-mercaptobenzothiazole matrix peak and taurocholate. Data was interpreted using Scils Lab MVS, Version 2021 c.

Gene expression analysis

RNA isolation and cDNA synthesis. Liver and kidney RNA was isolated from milled frozen tissue using the RNeasy Mini Kit, according to the manufacturer's protocol. cDNA synthesis was performed from 2 µg of isolated RNA using the High-Capacity cDNA Reverse Transcription Kit. ***qRT-PCR assays.*** qRT-PCR analyses were performed with cDNA using TaqMan 7500 Real-Time PCR, TaqMan universal PCR Master Mix, and

TaqMan gene expression assays (Table S5) (ThermoFisher Scientifics, Oberhausen, Germany). The gene expression values were normalized to the housekeeping gene GAPDH and further calculated with the ΔΔCt method. The values were expressed as fold changes over control samples.

RNA-sequencing and bioinformatics. RNA-seq of liver and kidney tissues was performed as previously described [21]. Transcript quantification of RNA-seq data and mapping of the FASTQ files were performed with the software Salmon, version 1.4.1, using the option 'partial alignment' and the online provided decoy-aware index for the mouse genome [22]. Further analyses were performed with R, version 4.2.2 [23]. To summarize the transcript reads on gene level, the R package tximeta was used [24]. For pre-filtering, genes with less than 10 reads across all mice (18,872) were removed, so that 16,855 genes remained for further analyses. The following analyses were performed separately for kidney and liver samples. Differential gene expression analysis was calculated using the R package DESeq2 [25]. A general linear model with one factor and levels "sham vehicle", "BDL vehicle" and "AS0369 BDL" was fitted to calculate differentially expressed genes (DEGs). DEGs were then calculated for the comparisons "sham vehicle vs. BDL vehicle" and "sham vehicle vs AS0369 BDL". For more reliable effect estimates, adaptive shrinkage was applied [26]. This leads to shrinkage of log-2 transformed fold-changes ($\log_2$(FCs)) towards zero if expression changes are mostly due to noise, whereas relevant $\log_2$(FCs) are preserved. For each comparison, a gene was considered to be differentially expressed if the effect size fulfils $\log_2(FC) > \log_2(1.5)$ for upregulation ($\log_2(FC) < -\log_2(1.5)$ for downregulation) and the estimate is significantly different from zero (i.e., no effect) with a false discovery rate (FDR)-adjusted p-value $p_{adj} < 0.05$. DiPa (Nell) plots were generated as recently described [27]. Enrichment analysis for biological processes gene ontology (GO) terms was applied separately for up and down regulated genes for the above described comparison "sham vehicle vs. BDL vehicle" and two of the areas defined in the differentiation pattern (DiPa) plot (Fig 7C, I) using the R package topGO [28]. P-values of GO groups were FDR-adjusted and considered significant if the adjusted p-value was smaller than 0.05. To compare DEGs between liver and kidney, Venn diagrams were used, and the corresponding overlap ratios were calculated as previously described [29]. The overlap ratio between two sets

of genes indicates the degree of overrepresentation in the overlap of the two gene sets compared to a random situation. If the ratio is higher than 1, the number of genes in the overlap is higher than randomly expected. The overlap ratio is calculated as follows: If $n_{universe}$ is the total number of analyzed genes, n_1 and n_2 are the numbers of DEGs in gene set 1 and 2, and O is the number of genes present in both sets, then: Overlap ratio = ($O \cdot n_{universe}$) / ($n_1 \cdot n_2$).

Statistical analysis. Mouse data. Data were analyzed using Prism software (GraphPad Prism 9.5.0 Software, Inc., La Jolla, CA, USA). Statistical group comparisons were done using Tukey's, Dunn's, or Šídák's multiple comparisons test, or unpaired t-test, as indicated in the figure legends. Statistical analysis of genome-wide gene expression was done using R (version 4.2.2) [23]. ***Serum data of liver disease patients and healthy volunteers.*** Correlation between sum bile acids, total bilirubin, and KIM-1 in serum was calculated by the Spearman correlation test. In the multiple linear regression analysis (stepwise backward selection) KIM-1 (pg/mL) was the dependent variable, while sum bile acids (µmol/L), total bilirubin (mg/dL), C-reactive protein (mg/dL), and UDCA therapy (yes, no) were tested as covariables. Mean arterial pressure (mmHg) was not analysed as a covariable, because only three patients showed values smaller than 70 mmHg. Differences in serum values between patients and controls were tested by the two-sided Wilcoxon test for unpaired data. The analyses were performed with SPSS version 29.

Supplementary video legends

Video S1: Reduced uptake of bile acids at the blood side of hepatocytes after bile duct ligation. A. Control mouse; **B.** Bile duct-ligated mouse (day 21). The time in the left corners indicates the minutes after TCA injection into the tail vein. Red: TMRE; green: TCA; blue: Hoechst. The videos correspond to Suppl. Fig. 2

Video S2: Zonated enrichment of TCA in renal tubular epithelial cells after bile duct ligation. A. Sham control mouse; **B.** Bile duct-ligated mouse (day 21) showing zonated enrichment of TCA in renal tubular epithelial cells (asterisk). The time in the left corners indicates the minutes after TCA injection into the tail vein. Red: TMRE; green: TCA; blue: Hoechst. The Videos correspond to Fig. 1A, B of the main manuscript.

Video S3: Time-resolved events after BDL. A. Intravital imaging of cell death (SYTOX green positive) of proximal tubular epithelial cells, release of cell debris into tubular lumen (example in the yellow circle) and cast formation in the distal tubules (white circles) and collecting ducts (blue circles). The proximal tubules are indicated by higher intensity of the mitochondrial potential marker TMRE. Green: SYTOX green; blue: Hoechst; red: TMRE. The video corresponds to Fig. 2C of the main manuscript. **B.** Intravital imaging of glomerular filtration of CLF (white circles) and leakage in the interstitial tissue of a 9-week BDL mouse. Note the dilatation of the Bowman's capsule after glomerular filtration of CLF (circles). Red: TMRE; green: CLF; blue: Hoechst. The video corresponds to Fig. 2B of the main manuscript.

Video S4: Renal peritubular capillary leakiness after BDL. Intravital imaging of Evans blue in 6-week sham-operated (A) or BDL (B) mice. Minutes after tail vein injection of Evans blue are given in the left corners. The videos show leakage of Evans blue into the interstitial tissue (asterisk) in the BDL but not in the sham-operated mouse. Magenta: Evans blue; blue: CD31 (endothelial cell marker). The videos correspond to Fig. 2E, F of the main manuscript.

Video S5: ASBT inhibition prevents the leakiness of renal capillaries after BDL. Intravital videos of mice after tail vein injection of Evans blue. **A.** sham + vehicle; **B.** A BDL mouse treated with vehicle showing leakage of Evans blue into the interstitial tissue (asterisk) within minutes after tail vein injection; **C.** BDL + AS0369. Magenta: Evans blue; blue: CD31. The videos correspond to Fig. 6D-G of the main manuscript.

Supplementary figures

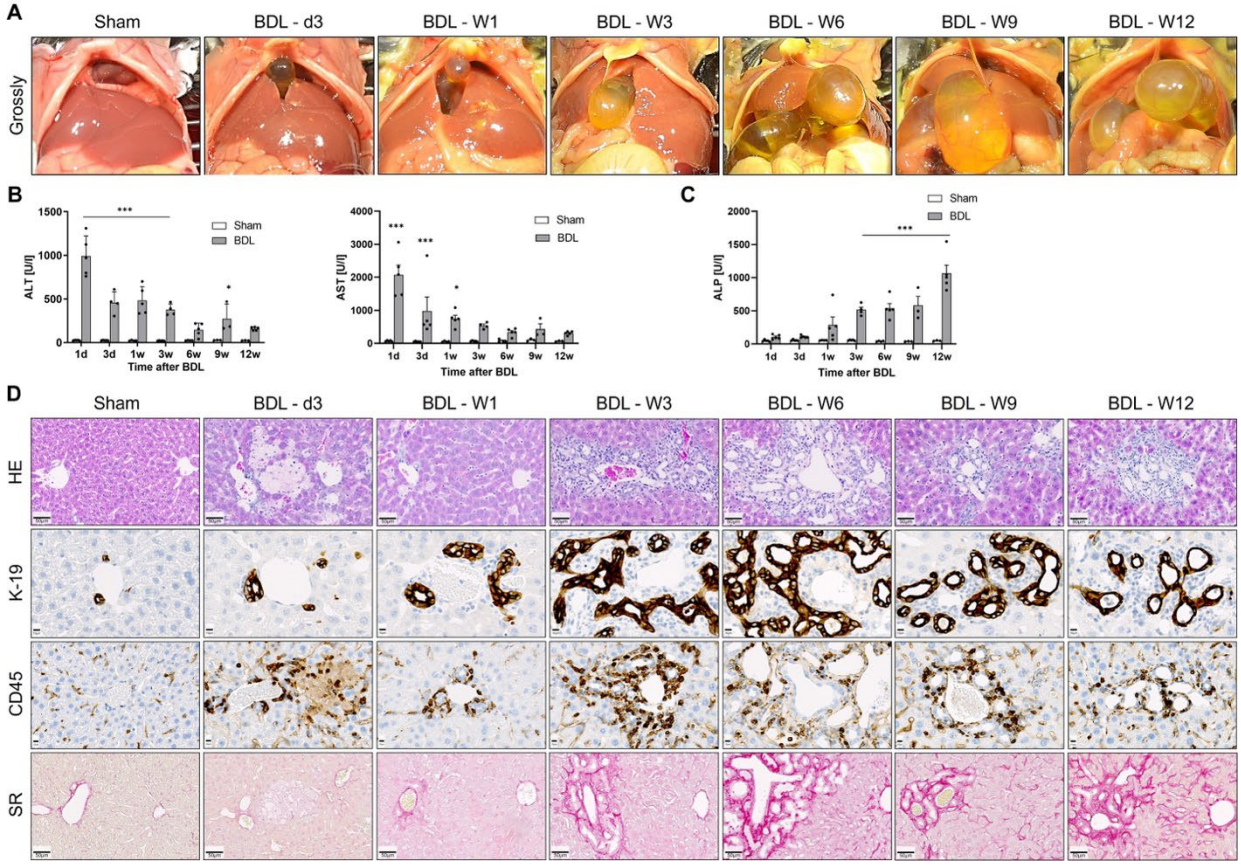

Fig. S1: Clinical chemistry and histology of the liver after BDL. A. Gross pathology. **B.** Plasma activities of ALT and AST. **C.** ALP activity. *p< 0.05; **p< 0.01; ***p< 0.001 compared to the corresponding sham controls, Šídák's multiple comparisons test. **D.** Histological analysis by hematoxylin and eosin (HE) staining (Scale bars: 50 µm), analysis for ductular reaction by the cholangiocyte marker K-19, immune cell infiltration by the pan-leukocyte marker CD45 (scale bars: 10 µm), and fibrosis as evidenced by Sirius red staining; scale bars: 50 µm.

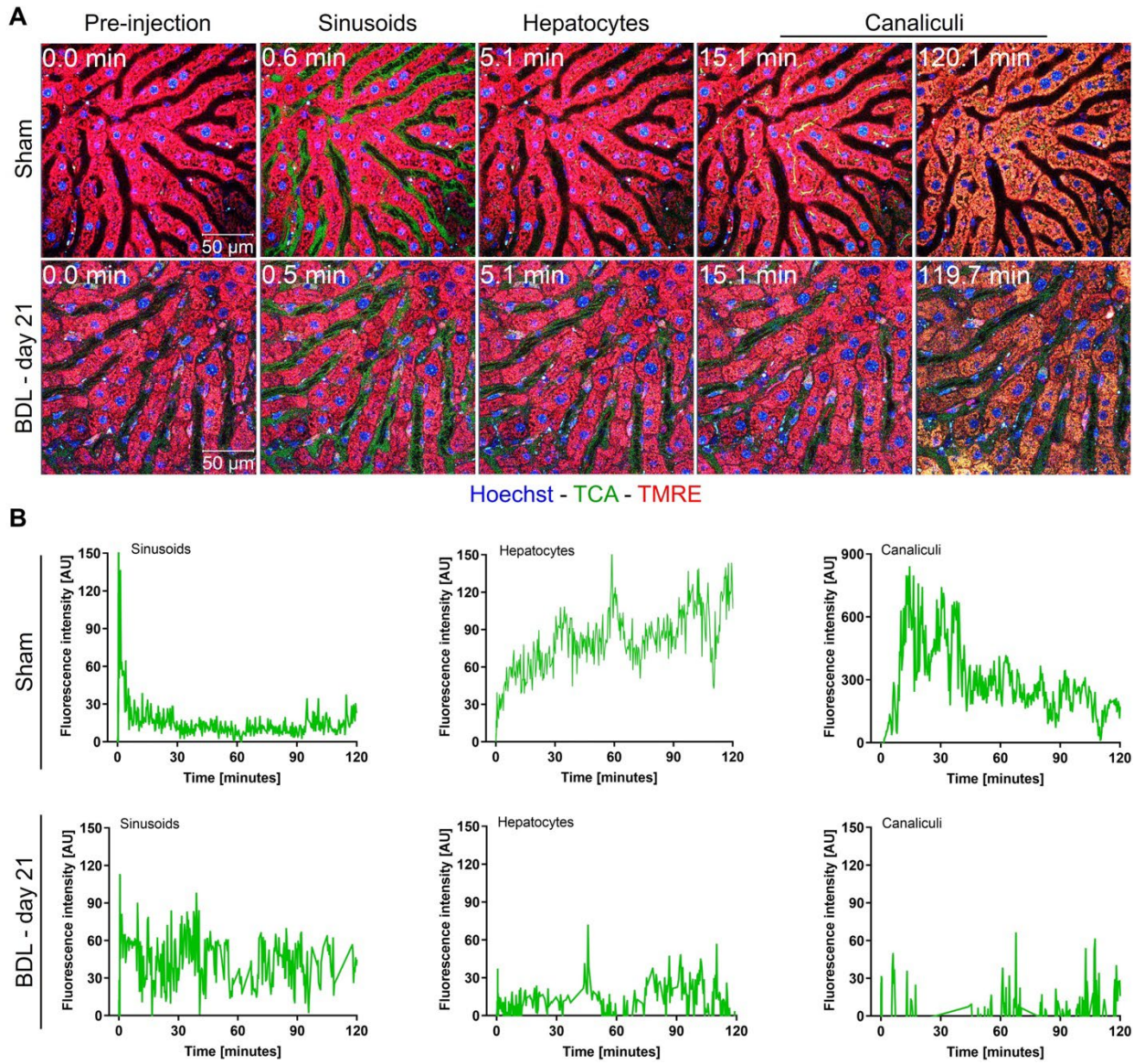

Fig. S2: Reduced uptake of bile acids at the blood side of hepatocytes after BDL. A. Stills from intravital videos in control mice (sham) and 21 days after BDL. The time indicates minutes after tail vein injection of fluorophore coupled TCA; scale bars: 50 µm; Red: TMRE; green: TCA; blue: Hoechst. The stills correspond to Suppl. Videos 1A and 1B. **B.** Quantification of the TCA signal in the blood sinusoids, hepatocytes, and bile canaliculi of the sham (upper panel) and the BDL (lower panel) mice.

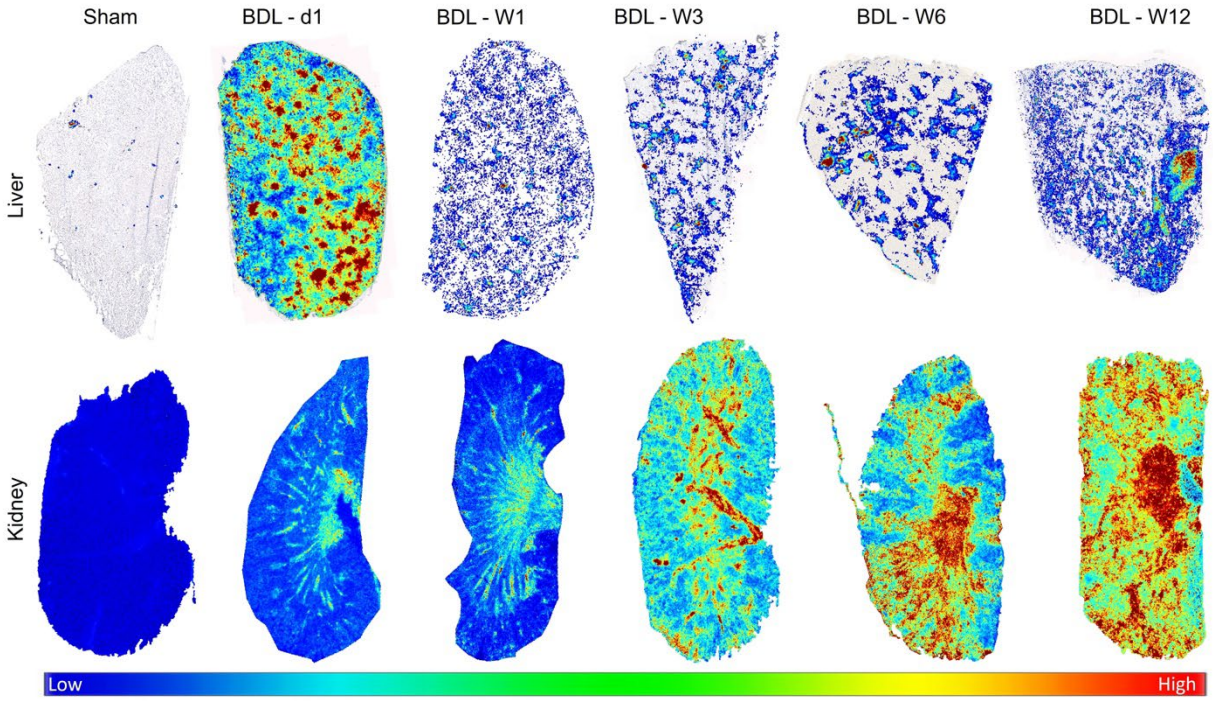

Fig. S3: Transient versus progressive enrichment of TCA in liver and kidney, respectively, after BDL. Cryosections of whole organ sections were analyzed by MALDI-MSI and the TCA signal was superimposed onto K-19 (liver, upper panel) or H&E (kidney, lower panel) staining. The corresponding quantifications are given in Fig. 1F of the main manuscript.

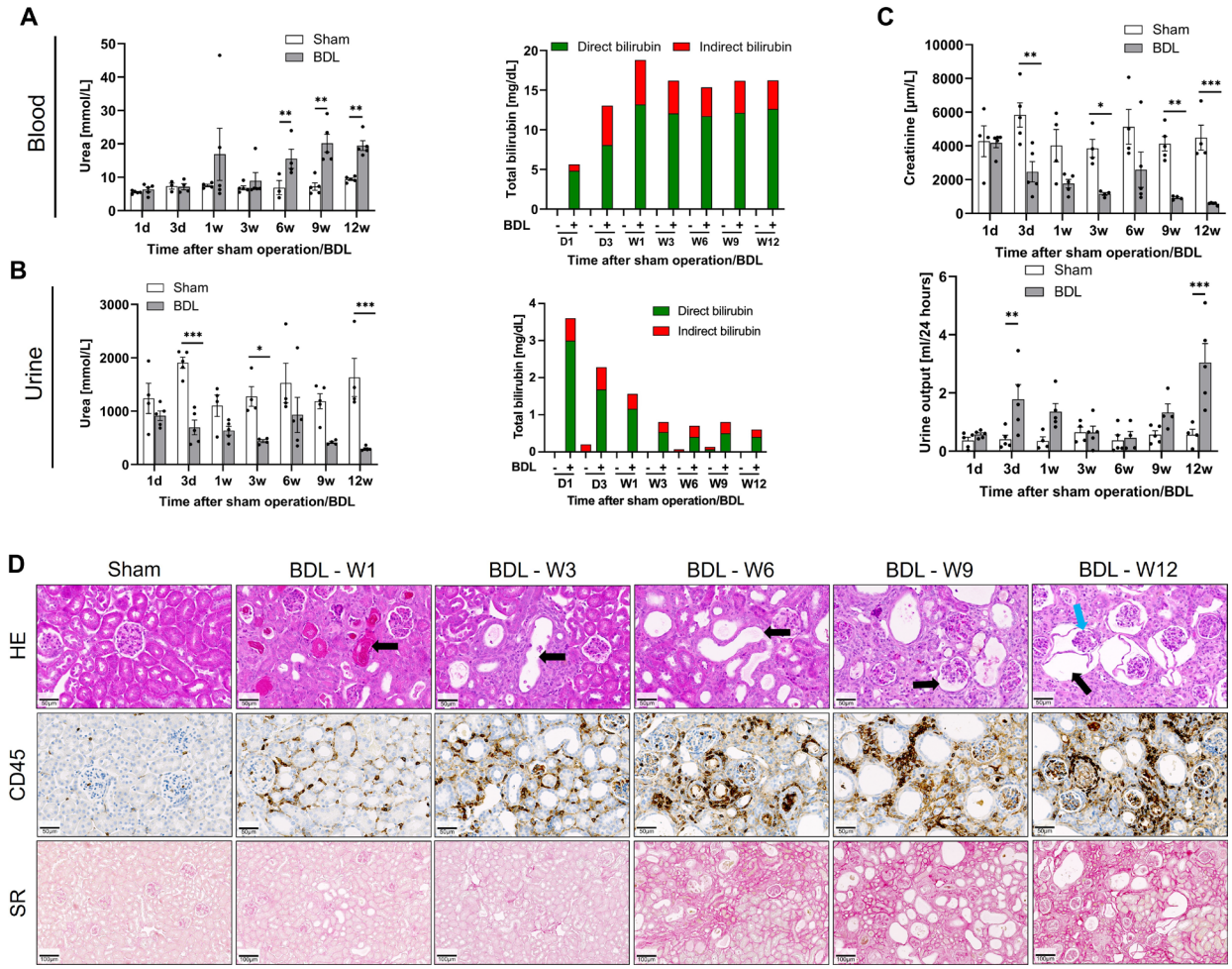

Fig. S4: A, B. Biomarkers of kidney injury in blood and in urine, and urine output; data are presented as means ± SEM; n= 5 mice per group. *p< 0.05; **p< 0.01; ***p< 0.001 compared to the corresponding sham controls, Šídák's multiple comparisons test. . **D.** Histology of the kidney after BDL. The images show the gross pathology; HE staining with cast formation (arrow on week 1), cystic dilatation of renal tubules (arrows at weeks 3 and 6), and glomerular cysts (arrows at weeks 9 and 12; the blue arrow at week 12 indicates atrophy of glomerular capillaries); the pan-leukocyte marker CD45 (scale bars: 50 µm); Hall's stain to visualize 'bile casts' in green (arrow; scale bars: 50 µm); and fibrosis based on Sirius red staining (scale bars: 100 µm).

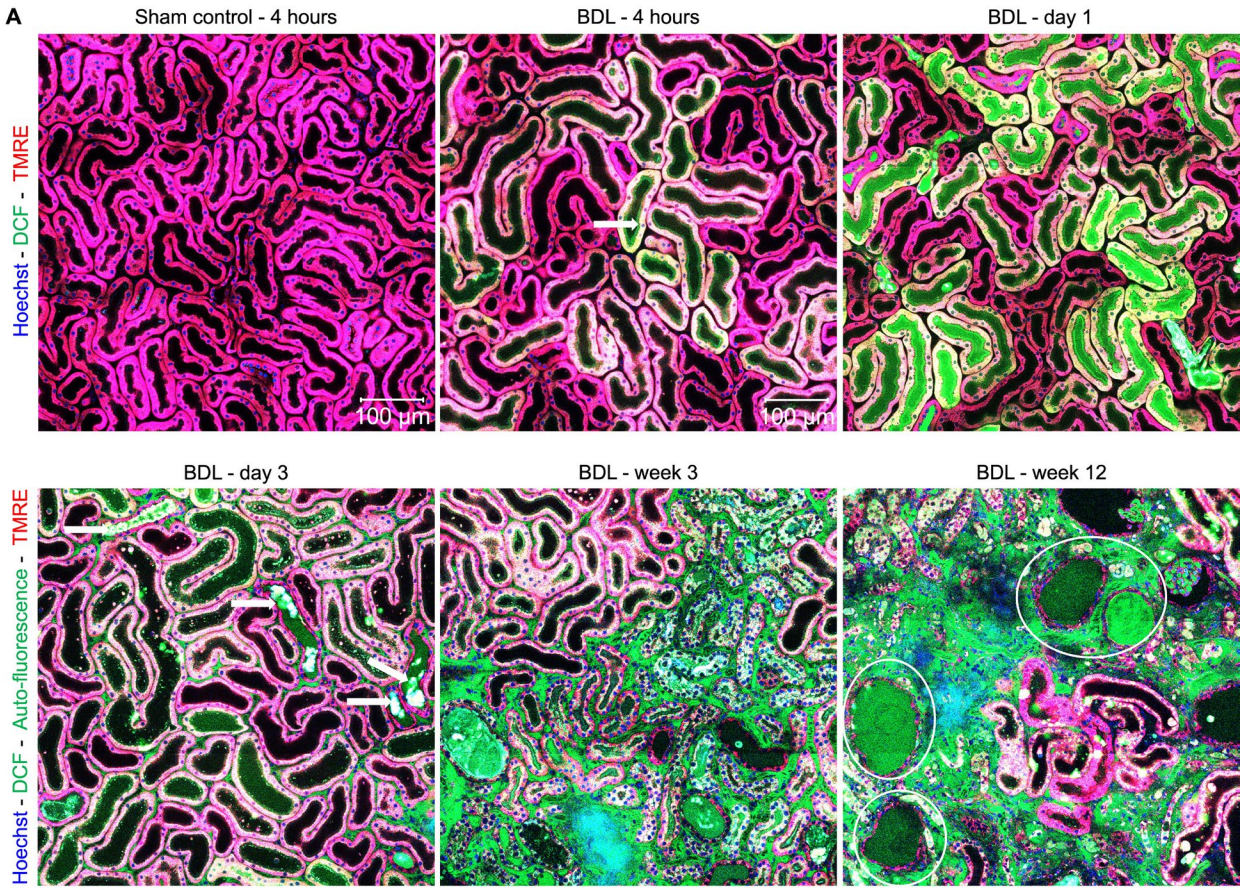

Fig. S5A: Sequence of events in the pathogenesis of cholemic nephropathy. Overview images of the kidneys at different time intervals after BDL showing the following sequence of events: (1) zonated oxidative stress in the proximal tubular epithelial cells (BDL 4 hours, arrow – day 1), (2) cell death of proximal tubular epithelial cells (days 1-3), (3) cast formation in distal tubules (day 3, arrows), (4) peritubular capillary leakiness (weeks 3 and 12), and (5) glomerular cysts (week 12, circles). Red: TMRE (the proximal TEC can be differentiated from distal tubules by their higher TMRE intensity); green: DCF (oxidative stress marker); blue: Hoechst; scale bars: 100 µm. The images correspond to Fig. 2B of the main manuscript.

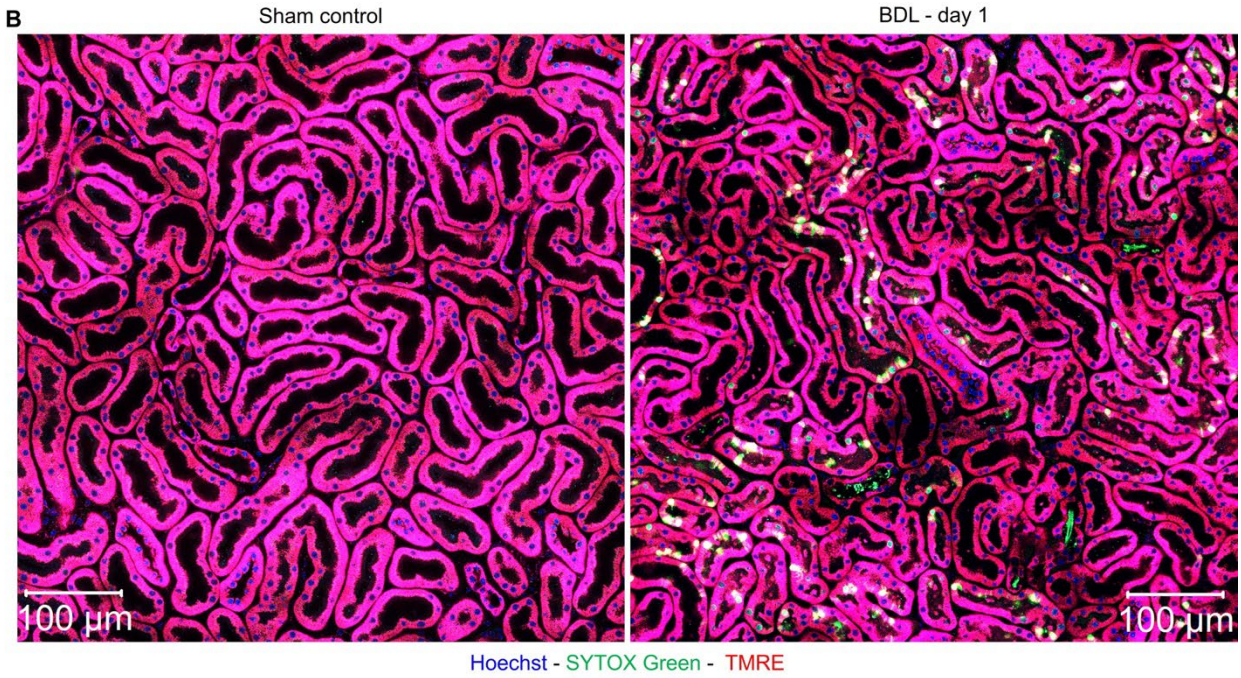

Fig. S5B: Zonation of cell death in proximal tubular epithelial cells on day 1 after BDL. The proximal tubular epithelial cells differ from the distal tubular epithelial cells by the higher intensity of the mitochondrial potential marker TMRE. Red: TMRE; green: SYTOX green (cell death marker); blue: Hoechst; scale bars: 100 µm. The images correspond to Fig. 2C of the main manuscript.

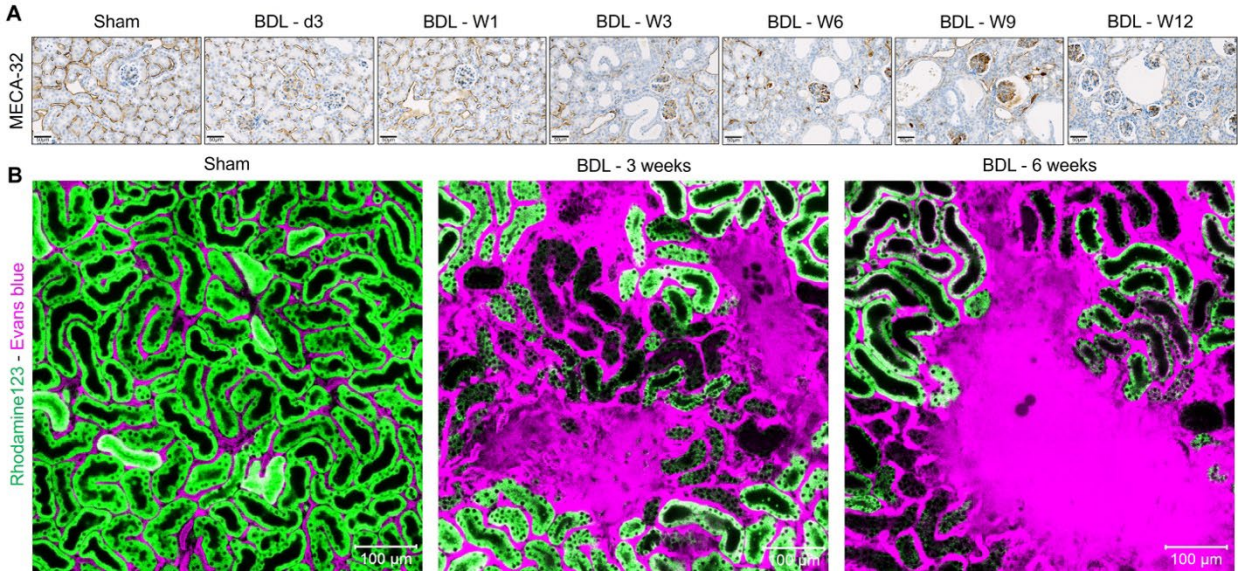

Fig. S6: Endothelial damage and leakiness of peritubular capillaries after BDL. A. Immunostaining with antibodies directed against the endothelial cell antigen MEC-32; scale bars: 50 µm. **B.** Intravital imaging after tail vein injection of Evans blue in control mice and 3 as well 6 weeks after BDL. Magenta: Evans blue; green: rhodamine123; scale bars: 100 µm.

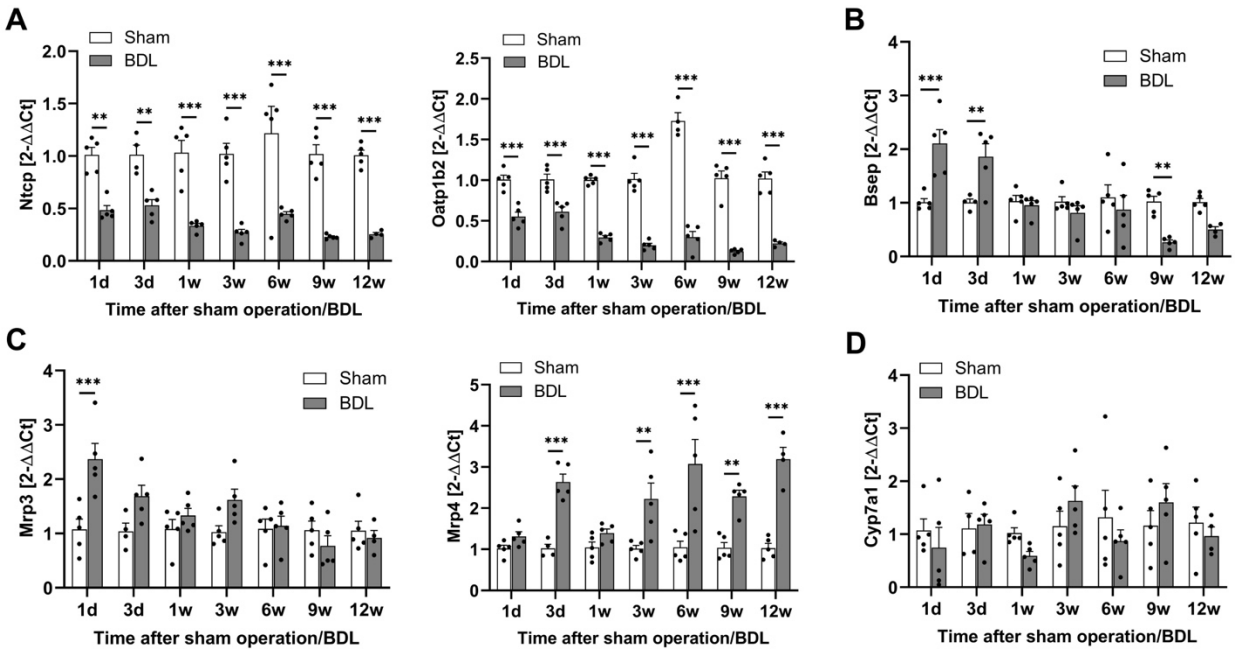

Fig. S7: Expression of bile acid transporters (A-C) and *Cyp7a1* (D) in the liver at different time intervals after BDL. **p< 0.01; ***p< 0.001 compared to the corresponding sham controls; Šídák's multiple comparisons test.

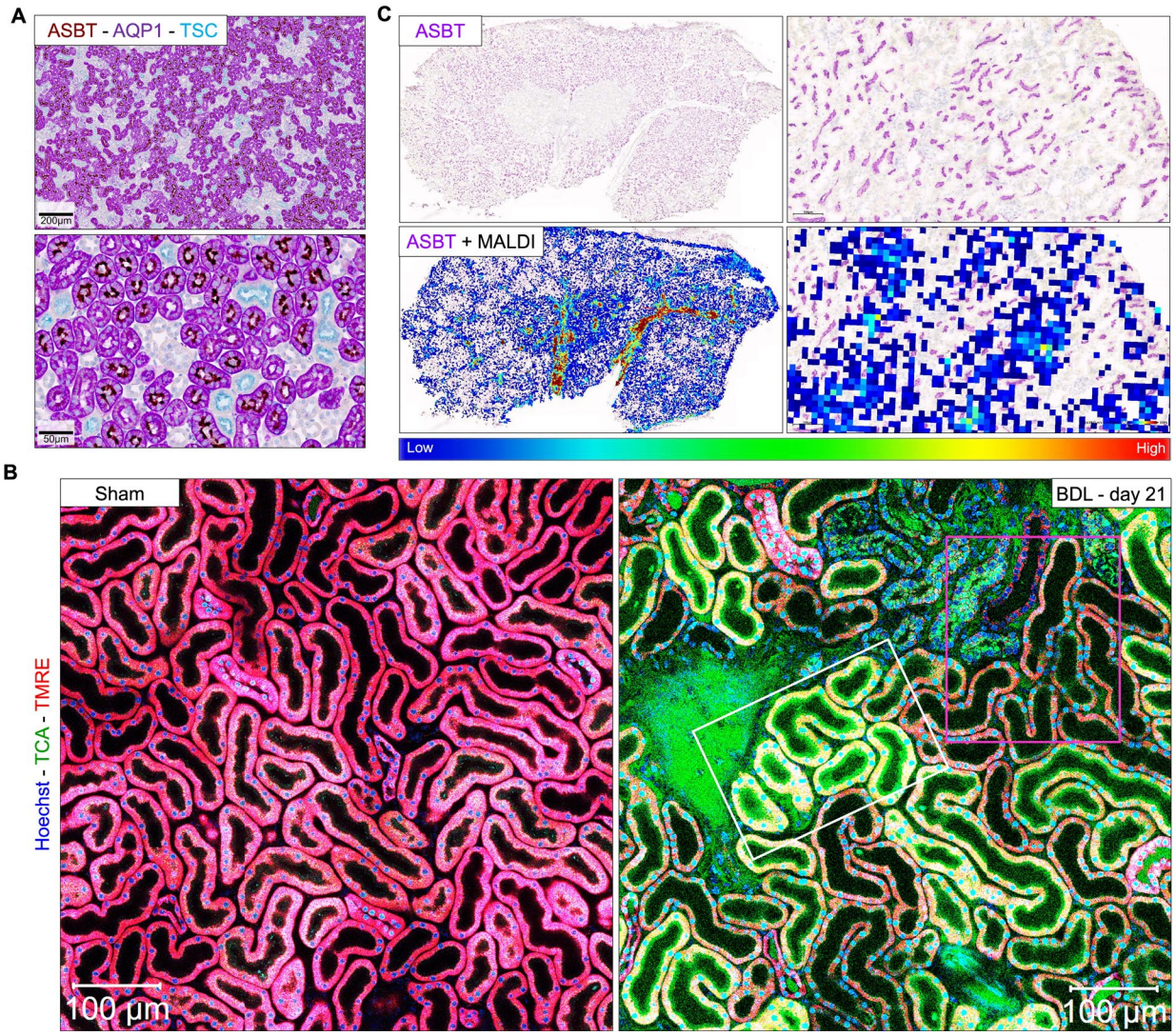

Fig. S8: Zonated expression of ASBT and bile acid uptake in renal tubular epithelial cells. **A.** Co-immunostaining of ASBT together with the proximal tubule marker AQP1 and the distal tubule marker TSC in renal tissue of control mice. **B.** Intravital imaging of fluorophore coupled TCA in the kidneys of control mice and of mice three weeks after BDL showing zonated enrichment of TCA in proximal (white rectangle) but not the distal (pink rectangle) tubular epithelial cells after BDL. **C.** MALDI-MSI imaging of TCA superimposed onto ASBT immunostaining in kidney tissue of a BDL mouse (day 1) showing zonated enrichment of TCA in regions with ASBT positive renal tubular epithelial cells.

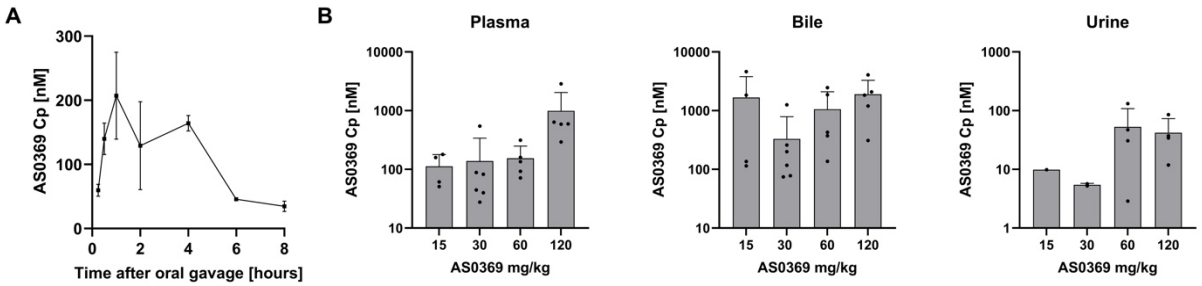

Fig. S9: A. Pharmacokinetics of AS0369 in wild-type mice after oral administration of 10 mg/kg. **B.** Plasma, bile and urinary concentrations of AS0369 in BDL mice after repeated twice daily oral application of various doses for 5 days; the analysis was done 4-7 hours after administration of the last dose of AS0369.

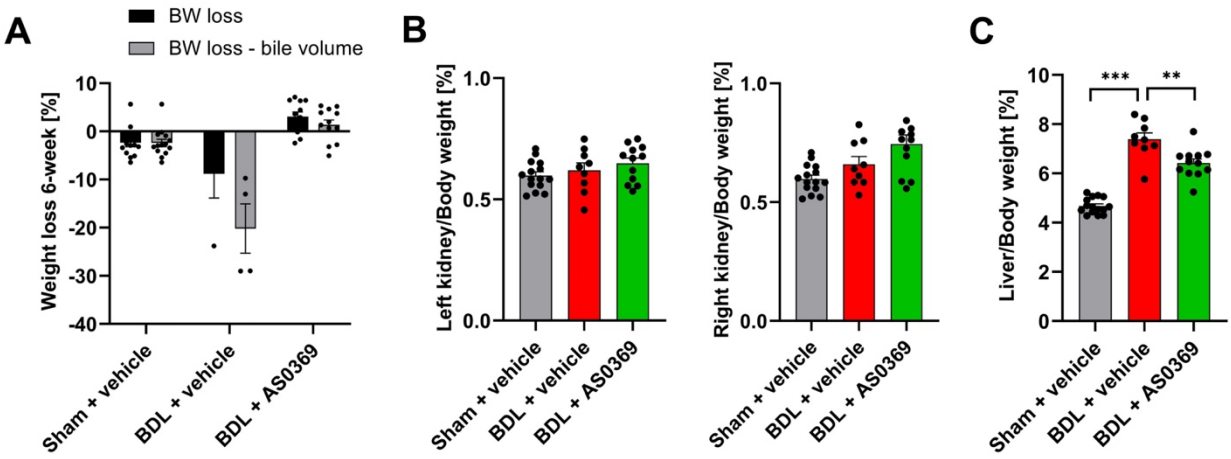

Fig. S10: A. Body weight of mice with BDL after administration of AS0369 or the vehicle, and sham operated mice with vehicle, with and without exclusion of the bile volume. **B, C.** Liver-to-body weight and kidney-to-body weight changes of mice with BDL after administration of AS0369 or the vehicle and sham operated mice with vehicle. **p< 0.01; ***p< 0.001 compared to the corresponding sham controls, Tukey's multiple comparisons test.

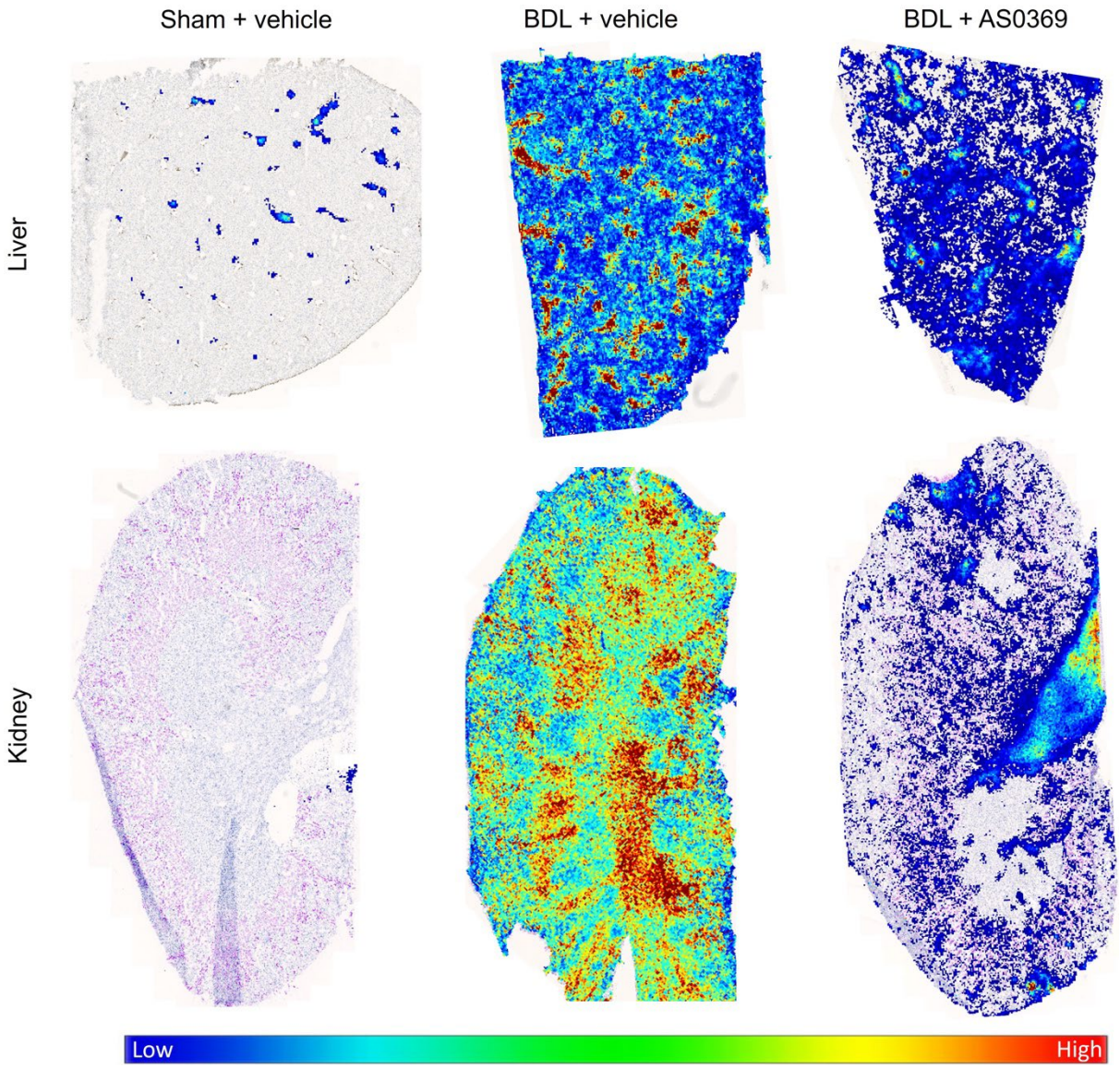

Fig. S11: ASBT inhibition reduces accumulation of bile acids in liver and kidney tissues after BDL. MALDI-MSI analysis of TCA was performed in mice of the three treatment groups illustrated in Fig 5A of the main manuscript. The upper panel shows the MALDI signal of TCA superimposed onto K-19 staining of liver tissue cryosections. The lower panel shows the MALDI signal of TCA superimposed onto ASBT staining of kidney tissue cryosections. The corresponding quantifications are given in Fig. 5H of the main manuscript.

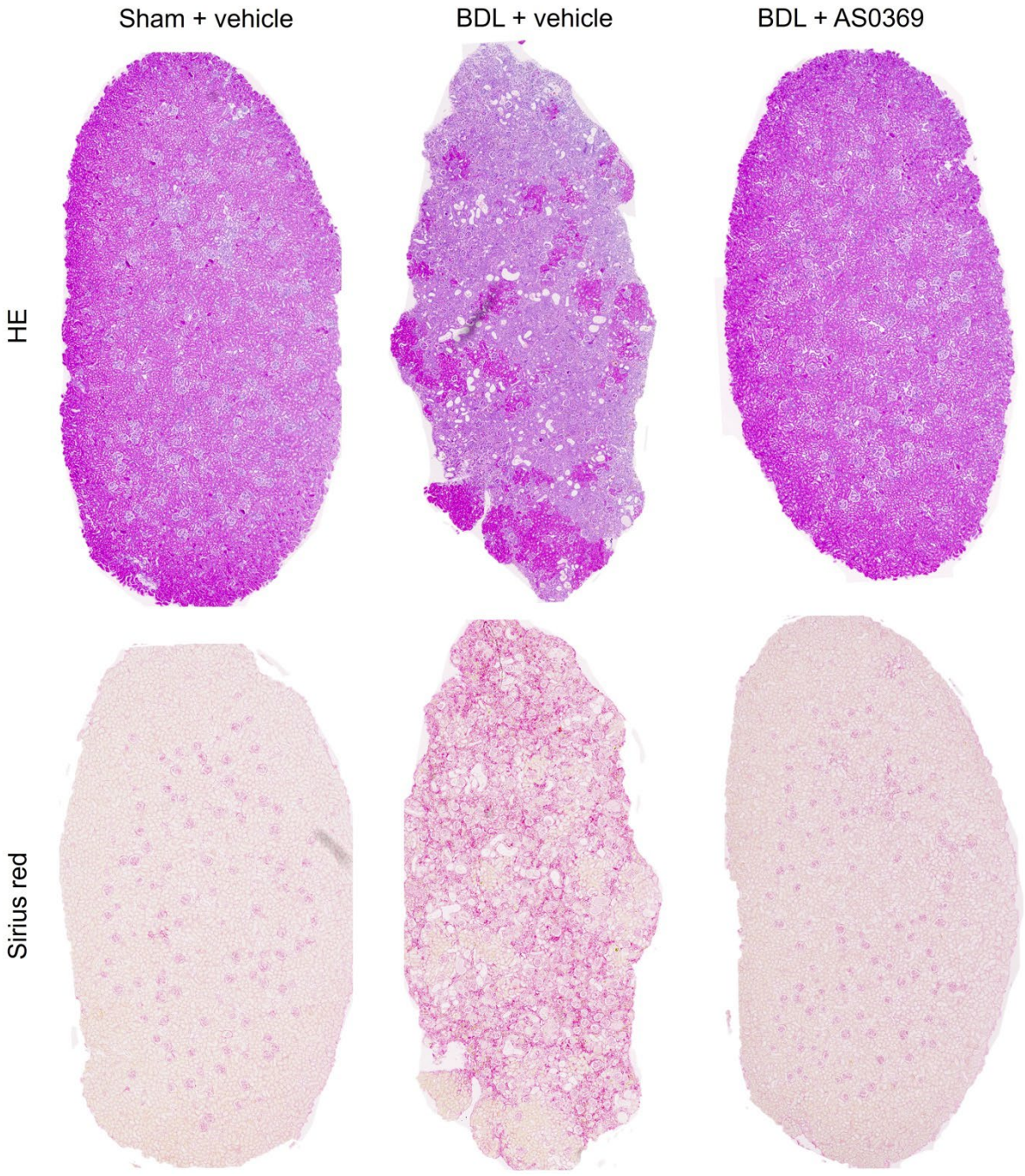

Fig. S12: ASBT inhibition prevents renal tubular epithelial cell damage and fibrosis. Whole organ sections of the kidney of mice according to the treatment schedule of Fig 5A stained with H&E (upper panel) and Sirius red (lower panel). The corresponding quantifications are given in Fig. 6B of the main manuscript.

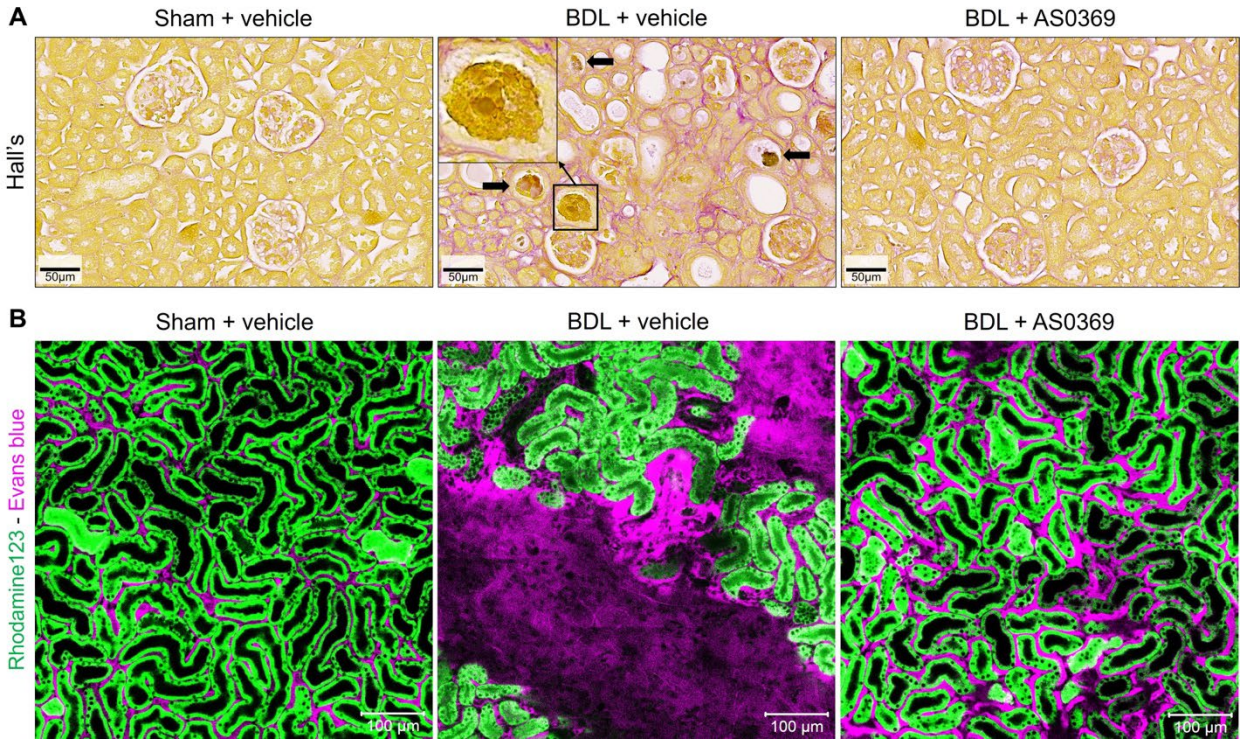

Fig. S13: ASBT inhibition prevents formation of Hall's positive bile casts and the leakiness of peritubular capillaries. A. Bile casts (arrows) visualized by Hall's stain; scale bars: 50 µm. **B.** Intravital imaging after tail vein injection of Evans blue (overviews); scale bars: 100 µm. The images correspond to the three treatment groups illustrated in Fig 5A of the main manuscript.

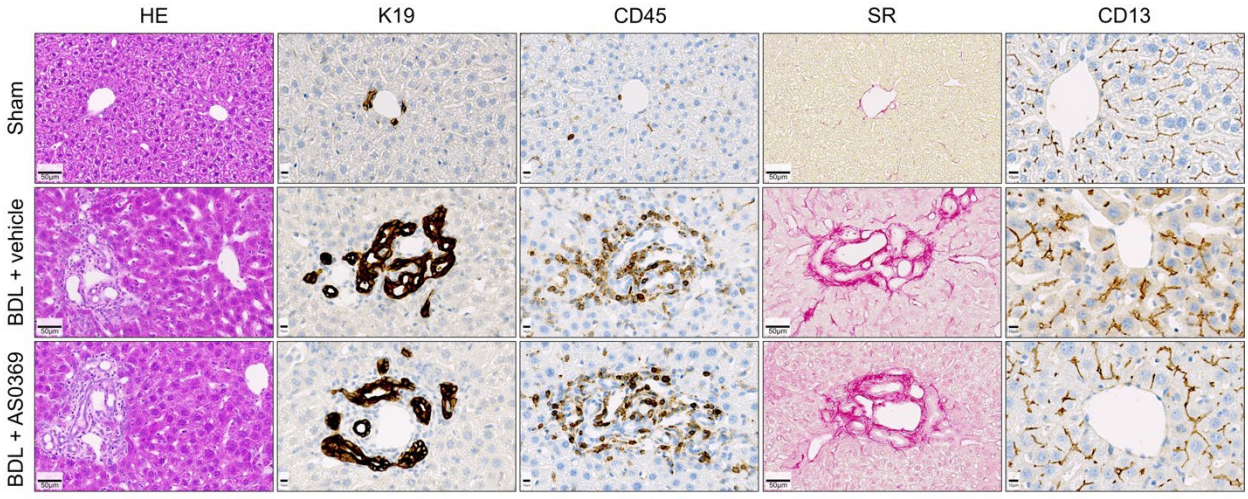

Fig. S14: Influence of ASBT inhibition on the liver. Histopathology (H&E and Sirius red), ductular reaction (K-19), leukocyte infiltration (CD45), and bile canaliculi (CD13) stainings; scale bars: 50 µm. The mice correspond to the three treatment groups illustrated in Fig 5A of the main manuscript.

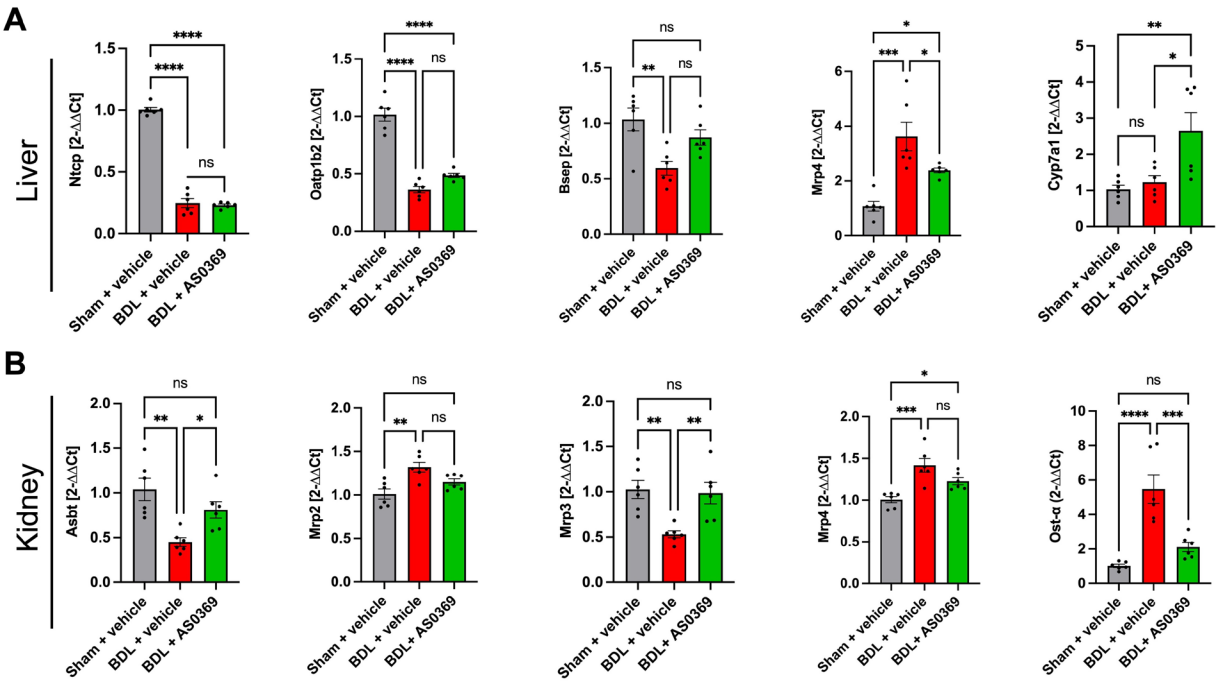

Fig. S15: RNA levels of bile acid carriers in liver and kidney tissue, and of *Cyp7a1* in the liver. The mice correspond to the three treatment groups illustrated in Fig 5A of the main manuscript. *p< 0.05; **p< 0.01; ***p< 0.001, ***p< 0.0001 compared to the sham controls, Dunn's multiple comparisons test.

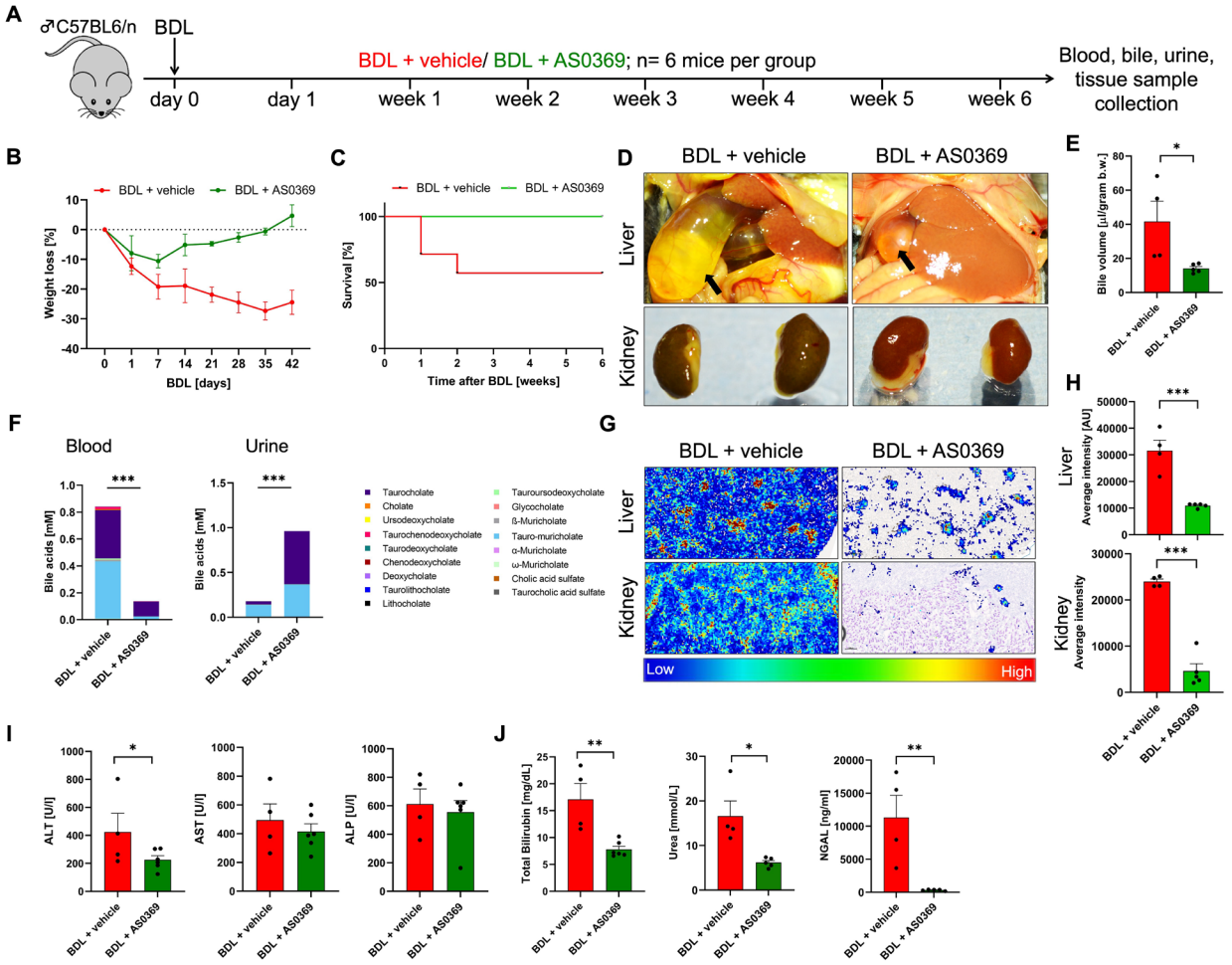

Fig. S16: Inhibition of ASBT prevents cholemic nephropathy in male mice after BDL. A. Experimental schedule. **B.** Bodyweight loss**. C.** Survival analysis**. D.** Gross pathology of the livers and kidneys**. E.** Gallbladder bile volume. **F.** Bile acid concentrations in blood and urine. **G, H.** MALDI-MSI of TCA in liver and kidney and corresponding quantifications. **I. J.** Clinical chemistry. *p< 0.05; **p< 0.01; ***p< 0.001 compared to the sham controls, Dunn's multiple comparisons test.

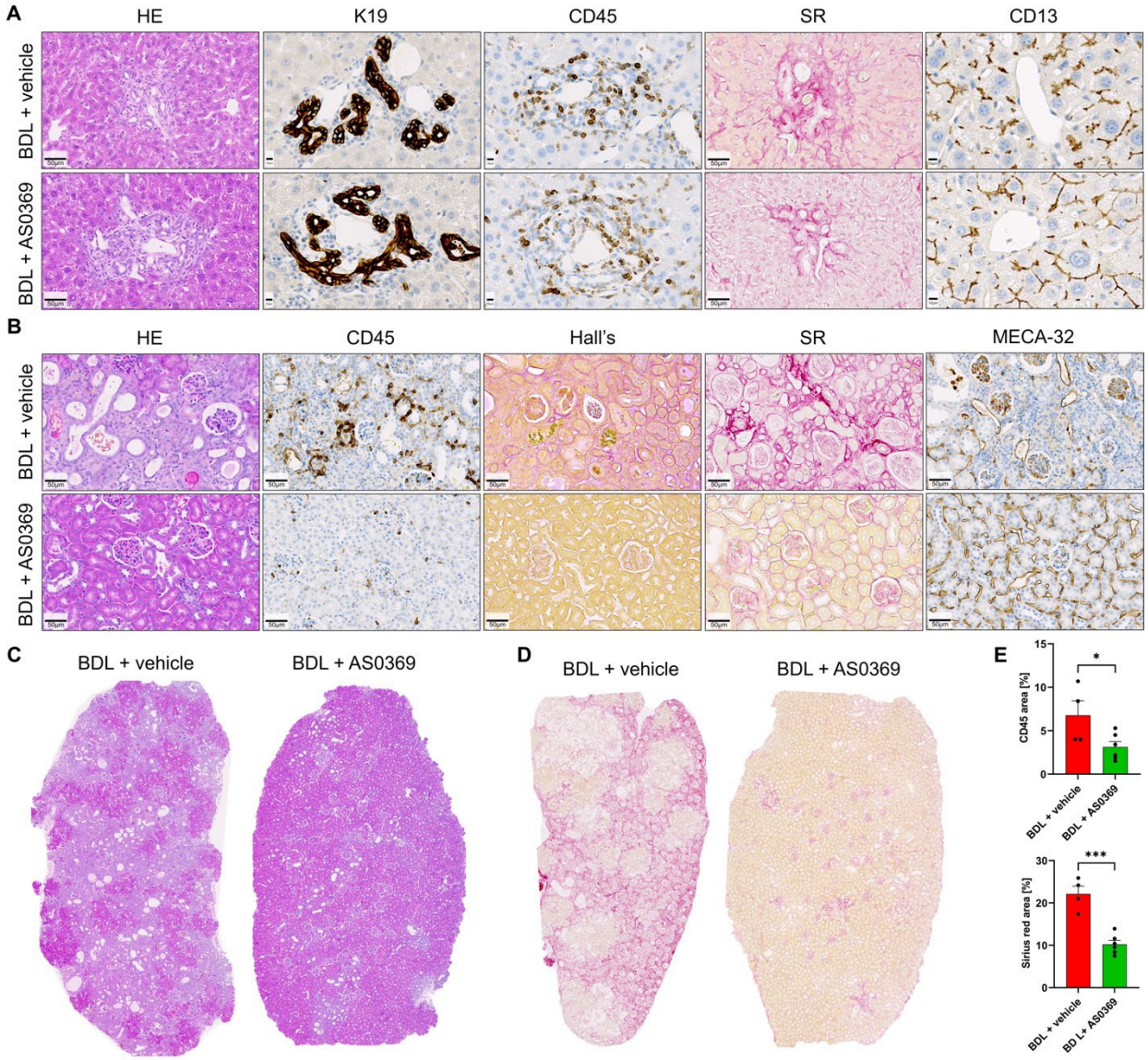

Fig. S17: Influence of ASBT inhibition on hepatic and renal histology. The treatment groups of the mice are illustrated in Suppl. Fig 17A. **A.** Liver histopathology. **B.** Kidney histopathology. **C-D.** Whole organ sections of the kidneys. **E.** Quantifications of CD45 and Sirius red signals in kidney tissue.

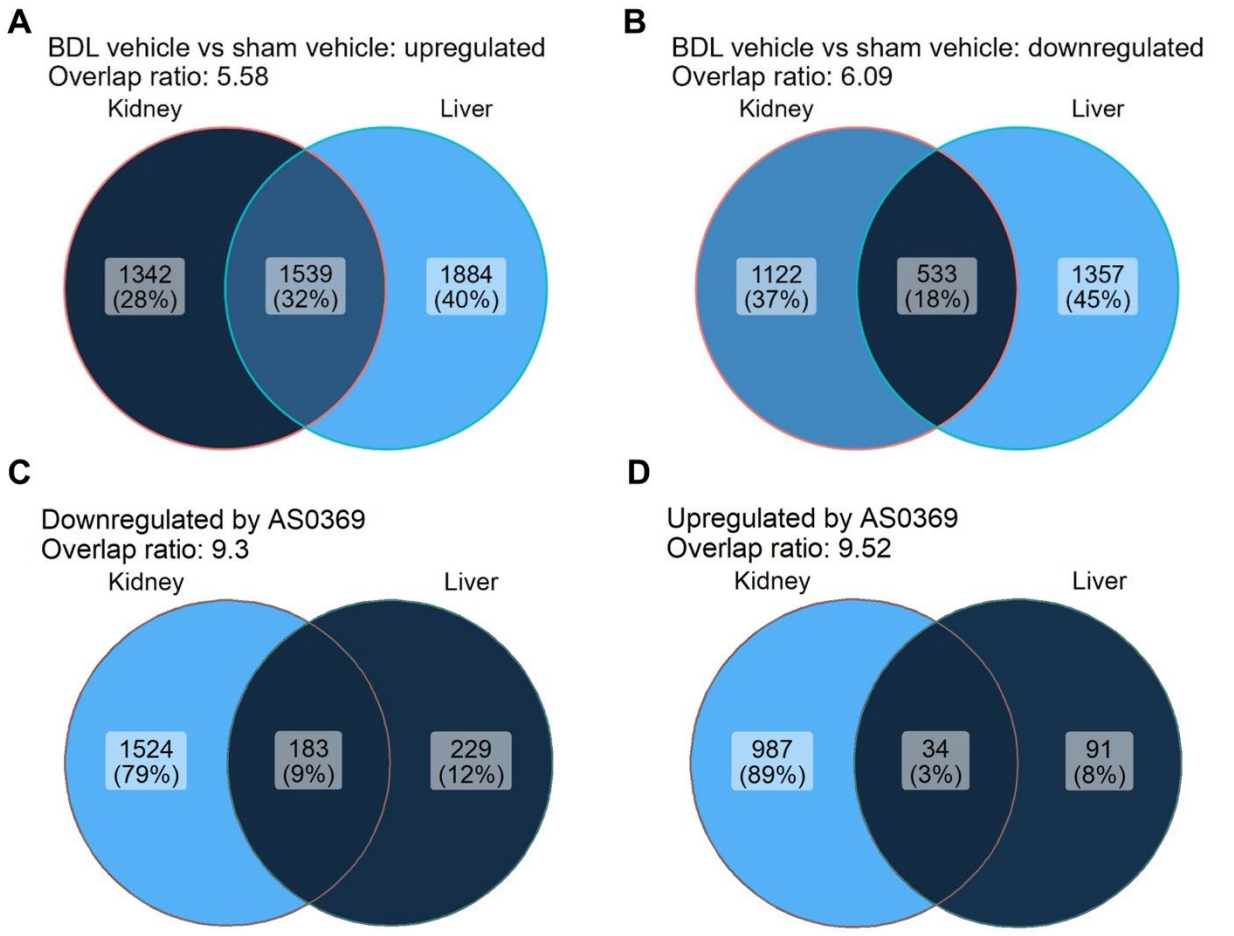

Fig. S18: Overlap analysis of differential genes in the kidney and liver. A. Overlap of up and downregulated genes due to BDL in kidney and liver. **B.** Overlap of the ASBT inhibitor (AS0369) response in the liver and kidney. The gene sets correspond to group 1a (left) and group 1b (right) of the DiPa plots shown in Fig 7C and 7I of the main manuscript. The overlap ratio indicates by which factor the number of genes in the overlap of both sets exceeds a randomly expected result.

Supplementary tables

Table S1A. Renal biopsies with and without cholemic nephropathy

Erlangen cohort				
n	**Sex**	**Age (years)**	**Disease**	**Serum creatinine (mg/dL)**
1	Male	49	Zero-time nephropathy	0.44
2	Female	61		0.62
3	Male	16		0.59
4	Female	57		0.78
5	Male	43		1.05
6	Male	24		0.98
7	Male	39		0.8
8	Male	63	Bile cast nephropathy	9
9	Male	75		7.9
10	Male	62		3.7
11	Male	62		3.8
12	Male	23		0.65
13	Male	52		3.53
14	Male	33		N.A.
Hannover cohort				
n	**Sex**	**Age (years)**	**Disease**	**Serum creatinine (mg/dL)**
1	Female	62	Zero-time nephropathy	N.A.
2	Female	64		N.A.
3	Female	68		N.A.
4	Female	56		N.A.
5	Male	54	Minimal Change	N.A.
6	Male	56		N.A.
7	Male	11		N.A.
8	Male	18		N.A.
9	Male	47		N.A.
10	Male	59	Cholemic Nephropathy	N.A.
11	Male	61		N.A.
12	Female	51		N.A.
13	Male	73		N.A.
14	Male	52		N.A.
15	Male	10		N.A.
16	Male	33		N.A.
17	Male	50		N.A.
18	Male	65		N.A.

Table S1B. Characteristics of patients with liver diseases and healthy volunteers

Patients (n=67) with liver disease and total bilirubin >6 mg/dL				Healthy volunteers (n=36) without known liver and kidney disease			P-value[1]
	Median	25%-Percentile	75%-Percentile	Median	25%-Percentile	75%-Percentile	
Age (years)	49.5	39.0	58.3	41.5	31.0	57.8	ns
Total bilirubin (mg/dL)	15.9	7.7	22.2	0.80	0.70	1.00	<0.001
Sum bile acids (µmol/L)	151.2	63.0	266.9	3.25	1.80	5.33	<0.001
KIM-1 (pg/mL)	805.1	582.1	1608.8	48.5	29.3	75.8	<0.001
NGAL (ng/mL)	102.5	55.6	199.9	65.5	51.3	83.0	0.009
Cystatin C (ng/mL)	1148.5	782.1	1643.0	806.5	700.5	958.0	<0.001
Creatinine (mg/L)	790	600	1010	850	800	1000	ns
AST (U/L)	98.0	69.0	171.0	22.0	20.0	26.0	<0.001
ALT (U/L)	56.0	42.0	115.0	17.5	14.0	21.0	<0.001
ALP (U/L)	160.0	103.0	248.0	60.5	54.0	69.0	<0.001
GGT (U/L)	133.0	56.0	286.0	15.5	12.0	24.5	<0.001
CRP (mg/dL)	1.86	0.48	3.42	nt	nt	nt	
Sex	Male: n=41 (61.2%); Female: n=26 (38.8%)			Male: n=13 (36.1%); Female: n=23 (63.9%)			
UDCA therapy	Yes: n=21 (31.3%); No: n=46 (68.7%)			no			
Mean arterial pressure (mmHg)	<65: n=2 (3.0%); ≥65: n=65 (97.0%)			nt			
Condition	• Alcoholic liver disease: n=30 (44.8%) • Acute liver injury: n=8 (11.9%) • Cholestatic liver disease: n=7 (10.4%) • Post-transplant: n=7 (10.4%) • Alcoholic liver disease plus viral: n=2 (3.0%) • NASH: n=3 (4.5%) • Hepatic malignancy: n=2 (3.0%) • Other: n=8 (12.0%)			none			

[1]P-value of the Wilcoxon test for independent variables, two-sided test, comparing patients and healthy volunteers. ns: not significant; nt: not tested.

Table S2: List of bile acids and internal standards with MRM transitions and MS parameters for quantification by LC-MS-MS.

Analyte	Internal Standard	Precursor Ion	Product Ion	CE (V)
ω-Muricholate (ωMCA)	d5-ωMCA	407.3	407.3	0
α-Muricholate (αMCA)	d5-αMCA	407.3	407.3	0
ß-Muricholate (ßMCA)	d5-βMCA	407.3	407.3	0
Tauro-α/ß-muricholate (TαßMCA)	d4-TßMCA	514.3	80.1	74
Tauro-ω-muricholate (TωMCA)	d4-TßMCA	514.3	80.1	74
7-Dehydrocholate (7-DHCA)	d4-TßMCA	405.3	405.3	38
Hyodesoxycholate (HDCA)	d4-UDCA	391.3	391.3	0
Cholate (CA)	d4-CA	407.3	343.4	36
Glycocholate (GCA)	d4-GCA	464.3	74.0	40
Taurocholate (TCA)	d4-TCA	514.3	80.1	74
Chenodeoxycholate (CDCA)	d4-CDCA	391.3	391.3	0
Taurochenodeoxycholate (TCDCA)	d4-TCDCA	498.3	80	80
Deoxycholate (DCA)	d4-DCA	391.3	345.3	32
Taurodeoxycholate (TDCA)	d4-TDCA	498.3	80.1	78
Ursodeoxycholate (UDCA)	d4-UDCA	391.3	391.3	0
Tauroursodeoxycholate (TUDCA)	d4-TUDCA	498.3	80.0	74
Lithocholate (LCA)	d5-LCA	375.3	375.3	0
Taurolithocholate (TLCA)	d4-TLCA	482.3	80.1	78
Cholic acid sulfate (CA-S)	d4-CA-S	487.2	96.9	58
Taurocholic acid sulfate (TCA-S)	d4-TCA-S	594.2	514.3	32
Internal Standard				
d5-ω-Muricholate (d5-ωMCA)		413.3	413.3	0
d5-α-Muricholate (d5-αMCA)		413.3	413.3	0
d5-ß-Muricholate (d5-ßMCA)		413.3	413.3	0
d4-Tauro-ß-muricholate (d4-TMCA)		518.3	80.1	74
d4-Cholate (d4-CA)		411.3	347.2	40
d4-Glycocholate (d4-GCA)		468.3	74.0	40
d4-Taurocholate (d4-TCA)		518.3	80.1	74
d4-Chenodeoxycholate (d4-CDCA)		395.3	395.3	0
d4-Taurochenodeoxycholate (d4-TCDCA)		502.3	80.0	86
d4-Deoxycholate (d4-DCA)		395.3	395.3	38
d4-Taurodeoxycholate (d4-TDCA)		502.3	80.0	82
d4-Ursodeoxycholate (d4-UDCA)		395.3	395.3	0
d4-Tauroursodeoxycholate (d4-TUDCA)		502.3	80.0	74
d5-Lithocholate (d5-LCA)		380.3	380.3	0
d4-Taurolithocholate (d4-TLCA)		486.3	80.1	90
d4-Cholic acid sulfate (d4-CA-S)		491.3	98.0	58
d4-Taurocholic acid sulfate (d4-TCA-S)		598.3	518.3	32

Table S3. Antibodies used for immunohistochemistry.

Target	Primary antibodies		Secondary antibodies	
	Antibody	Dilution	Antibody	Dilution
Cholangiocyte	Anti-cytokeratin 19 antibody, rabbit	1:500	Ultra-Map anti rabbit HRP	Automatic Discovery Ready to use
Bile canaliculi	Recombinant anti-CD13 antibody, rabbit	1:16000	Ultra-Map anti rabbit HRP	
Leukocytes	Anti-CD45 antibody, rat	1:400	Omni-Map anti rat HRP	
Endothelial cells	Anti-MECA-32 antibody, rat	1:250	Ultra-Map anti rat HRP	
ASBT	Anti-ASBT antibody, goat	1:500	Ultra-Map anti goat HRP	
ASBT	Anti-ASBT antibody, rabbit	1:50	Ultra-Map anti rabbit HRP	
AQP1	Anti-AQP1 antibody, rabbit	1:10000	Ultra-Map anti rabbit HRP	
TSC	Anti-TSC antibody, rabbit	1:2000	Ultra-Map anti rabbit HRP	

Table S4. Fluorescent markers and functional dyes used in the study.

Fluorescent marker	Marker for	Dose [mg/kg]	Vehicle	Two-photon excitation range [nm]
Hoechst 33258	Nuclei	5	PBS	700-800
TMRE	mitochondrial membrane potential	0.96	Methanol: PBS (1:1)	740-820
Cholyl-lysyl-fluorescein	Bile acid analogue	1	PBS	740-820
2',7'Dichlorofluorescein diacetate	Oxidative stress	0.5	DMSO	900-950
SYTOX green	Cell death	1.2	DMSO: PBS (1:100)	900-950
Fluorescein-coupled TCA	Bile acid analogue	1	PBS	740-820
Fluorescent marker	**Marker for**	**Dose [mg/kg]**	**Vehicle**	**Confocal excitation range [nm]**
Anti-CD31	Endothelial cells	0.08	PBS	381 - 459
Evans blue	Capillary leakiness	0.5	PBS	646 - 709
Rhodamine123	Mitochondrial membrane potential	0.8	Methanol: PBS (1:1)	498 - 532

Table S5. TaqMan gene assays.

Gene	TaqMan Assay ID
Abcb11	Mm00445168_m1
Abcc2	Mm00496899_m1
Abcc3	Mm00551550_m1
Abcc4	Mm01226381_m1
Cyp7a1	Mm00484150_m1
Egr1	Mm00656724_m1
GAPDH	Mm99999915_g1
Slc1a2	Mm01275814_m1
Slc10a1	Mm00441421_m1
Slc10a2	Mm00488258_m1
Slco1b2	Mm00451510_m1
Slc51a	Mm00521530_m1

Supplementary references

[1] Ghallab A, Hofmann U, Sezgin S, Vartak N, Hassan R, Zaza A, et al. Bile Microinfarcts in Cholestasis Are Initiated by Rupture of the Apical Hepatocyte Membrane and Cause Shunting of Bile to Sinusoidal Blood. Hepatology 2019;69:666-683.

[2] Tag CG, Sauer-Lehnen S, Weiskirchen S, Borkham-Kamphorst E, Tolba RH, Tacke F, et al. Bile duct ligation in mice: induction of inflammatory liver injury and fibrosis by obstructive cholestasis. J Vis Exp 2015.

[3] Ghallab A, Celliere G, Henkel SG, Driesch D, Hoehme S, Hofmann U, et al. Model-guided identification of a therapeutic strategy to reduce hyperammonemia in liver diseases. J Hepatol 2016;64:860-871.

[4] Gianmoena K, Gasparoni N, Jashari A, Gabrys P, Grgas K, Ghallab A, et al. Epigenomic and transcriptional profiling identifies impaired glyoxylate detoxification in NAFLD as a risk factor for hyperoxaluria. Cell Rep 2021;36:109526.

[5] Reis LO, Sopena JM, Fávaro WJ, Martin MC, Simão AF, Reis RB, et al. Anatomical features of the urethra and urinary bladder catheterization in female mice and rats. An essential translational tool. Acta Cir Bras 2011;26 Suppl 2:106-110.

[6] Leuthold P, Schaeffeler E, Winter S, Büttner F, Hofmann U, Mürdter TE, et al. Comprehensive Metabolomic and Lipidomic Profiling of Human Kidney Tissue: A Platform Comparison. J Proteome Res 2017;16:933-944.

[7] Holland CH, Ramirez Flores RO, Myllys M, Hassan R, Edlund K, Hofmann U, et al. Transcriptomic Cross-Species Analysis of Chronic Liver Disease Reveals Consistent Regulation Between Humans and Mice. Hepatol Commun 2022;6:161-177.

[8] Hall MJ. A staining reaction for bilirubin in sections of tissue. Am J Clin Pathol 1960;34:313-316.

[9] Ghallab A, Hassan R, Hofmann U, Friebel A, Hobloss Z, Brackhagen L, et al. Interruption of bile acid uptake by hepatocytes after acetaminophen overdose ameliorates hepatotoxicity. J Hepatol 2022;77:71-83.

[10] Hassan R, Gonzalez D, Hobloss Z, Brackhagen L, Myllys M, Friebel A, et al. Inhibition of cytochrome P450 enhances the nephro- and hepatotoxicity of ochratoxin A. Arch Toxicol 2022;96:3349-3361.

[11] Zuiderveld K. Contrast Limited Adaptive Histogram Equalization. In: Paul S Heckbert (Hg): Graphics gems [IBM-ausg], 5 [Dr] Boston: Academic Press (The graphic gems series), S 474–485 2000.

[12] Friebel A, Johann T, Drasdo D, Hoehme S. Guided interactive image segmentation using machine learning and color-based image set clustering. Bioinformatics 2022;38:4622-4628.

[13] Breiman L. Machine Mearning 2001;45:5.

[14] Bankhead P, Loughrey MB, Fernández JA, Dombrowski Y, McArt DG, Dunne PD, et al. QuPath: Open source software for digital pathology image analysis. Sci Rep 2017;7:16878.

[15] Durix B, Chambon S, Leonard K, Mari J-L, Morin G. The Propagated Skeleton: A Robust Detail-Preserving Approach. In: Couprie M, Cousty J, Kenmochi Y, Mustafa N, editors. Discrete Geometry for Computer Imagery; 2019 2019//; Cham: Springer International Publishing; 2019. p. 343-354.

[16] Ghallab A, Hassan R, Myllys M, Albrecht W, Friebel A, Hoehme S, et al. Subcellular spatio-temporal intravital kinetics of aflatoxin B(1) and ochratoxin A in liver and kidney. Arch Toxicol 2021;95:2163-2177.
[17] **Reif R, Ghallab A**, Beattie L, Gunther G, Kuepfer L, Kaye PM, et al. In vivo imaging of systemic transport and elimination of xenobiotics and endogenous molecules in mice. Arch Toxicol 2017;91:1335-1352.
[18] Vartak N, Guenther G, Joly F, Damle-Vartak A, Wibbelt G, Fickel J, et al. Intravital Dynamic and Correlative Imaging of Mouse Livers Reveals Diffusion-Dominated Canalicular and Flow-Augmented Ductular Bile Flux. Hepatology 2021;73:1531-1550.
[19] Bábíčková J, Klinkhammer BM, Buhl EM, Djudjaj S, Hoss M, Heymann F, et al. Regardless of etiology, progressive renal disease causes ultrastructural and functional alterations of peritubular capillaries. Kidney Int 2017;91:70-85.
[20] Thévenaz P, Ruttimann UE, Unser M. A pyramid approach to subpixel registration based on intensity. IEEE Trans Image Process 1998;7:27-41.
[21] Ghallab A, Myllys M, Friebel A, Duda J, Edlund K, Halilbasic E, et al. Spatio-Temporal Multiscale Analysis of Western Diet-Fed Mice Reveals a Translationally Relevant Sequence of Events during NAFLD Progression. Cells 2021;10.
[22] Patro R, Duggal G, Love MI, Irizarry RA, Kingsford C. Salmon provides fast and bias-aware quantification of transcript expression. Nature Methods 2017;14:417-419.
[23] Team RC. R: A language and environment for statistical computing. R Foundation for Statistical Computing, Vienna, Austria https://wwwR-projectorg/ 2022.
[24] Love MI, Soneson C, Hickey PF, Johnson LK, Pierce NT, Shepherd L, et al. Tximeta: Reference sequence checksums for provenance identification in RNA-seq. PLoS Comput Biol 2020;16:e1007664.
[25] Love MI, Huber W, Anders S. Moderated estimation of fold change and dispersion for RNA-seq data with DESeq2. Genome Biology 2014;15:550.
[26] Zhu A, Ibrahim JG, Love MI. Heavy-tailed prior distributions for sequence count data: removing the noise and preserving large differences. Bioinformatics 2019;35:2084-2092.
[27] **Nell P, Kattler K, Feuerborn D**, Hellwig B, Rieck A, Salhab A, et al. Identification of an FXR-modulated liver-intestine hybrid state in iPSC-derived hepatocyte-like cells. J Hepatol 2022;77:1386-1398.
[28] Alexa A, Rahnenführer J, Lengauer T. Improved scoring of functional groups from gene expression data by decorrelating GO graph structure. Bioinformatics 2006;22:1600-1607.
[29] **Shinde V, Hoelting L**, Srinivasan SP, Meisig J, Meganathan K, Jagtap S, et al. Definition of transcriptome-based indices for quantitative characterization of chemically disturbed stem cell development: introduction of the STOP-Tox(ukn) and STOP-Tox(ukk) tests. Arch Toxicol 2017;91:839-864.

Author names in bold designate shared co-first authorship.